Geometric Improvement of a Perimetric Exhaust

Miguel Alexandre Fechado

Thesis to obtain the Master of Science Degree in

Mechanical Engineering

Supervisors: Prof. Edgar Caetano Fernandes
Prof. Luís Rego da Cunha de Eça

Examination Committee

Chairperson: Prof. Carlos Frederico Neves Bettencourt da Silva
Supervisor: Prof. Edgar Caetano Fernandes
Member of the Committee: Prof. Miguel Abreu de Almeida Mendes

November 2019

Dedicated to Jules and Anthoine

Acknowledgments

First of all, I would like to express my deep appreciation to Professors Edgar Caetano Fernandes and Luís Rego da Cunha da Eça, for all the help, support and guidance along this work. Without the sharing of their knowledge during the thesis but also in the classes given along the course, this work would not have been possible.

To engineer António Viegas, for his valuable input and support. To Sandra Dias, Laboratory Manager, for the help given every time it was requested, Alexandre Ferro and Ivo Monteiro, for the availability to answer any questions and the work that both have made and precedes this thesis, and João Cunha, whom provided an essential code to retrieve the experimental data of this work.

To all the colleagues who were side by side with me in the laboratory and helped whenever needed: João Xavier, Rui Araújo, Miguel Ribeiro, André Korolev, Mafalda Medeiros, Muhammad Ferdous Raiyan, Miguel Santos, Alexandre Gambôa, Miguel Figueiredo, Gonçalo Granjal, Pedro Pontes, Ricardo Cautela, Eduardo Freitas and Pedro Santos.

To everyone who was with me in the Projecto FST Novabase/FST Lisboa team, specially the boys from the Chassis department, thank you for inspiring me when I most needed, making me realise why I was got into this course and helping me to work harder and chase my goals.

To the closest colleagues I met in this course, who have now become friends for life and helped me countless times during the last six years: Gonçalo Sousa, Afonso Mocho, Manuel Gambôa, Miguel Chastre, Pedro Prata, Marta Rocha, Francisco Espenica. A special thanks to Filipa Neves and Sofia Torres, for all the support in the final stages of this work. Thank you all.

To all the friends I met back home and are still with me, thank you for growing up with me and sharing our lives together. To all the new friends I met in Lisbon and helped me go through this experience. And last but not least, to my family, who always believed in me, even when I didnt't. For all the support through bad times and good times. And for being the source of energy when there was none left.

This work was developed at the Thermofluids, Combustion and Energy Systems laboratory of the IN+ - Center for Innovation, Technology and Policy Research.

Resumo

A presente dissertação foca-se na melhoria da geometria dos canais no interior de um exaustor perimetral, com o objectivo de melhorar a sua eficiência energética e de filtragem de gorduras. Isto é feito através de simulações numéricas em 2D, com uma parte experimental para avaliar os resultados do estudo computacional.

A geometria inicial foi estudada como base para comparação com as novas versões, mas também para determinar como é que diferentes características do escoamento (bolhas de recirculação) variam com a velocidade de entrada no canal e temperatura de funcionamento do exaustor. De seguida, duas primeiras versões foram testadas. Ambas tiveram melhores resultados que a geometria inicial. A melhor destas sofreu três novas iterações para maximizar as melhorias do seu desempenho, com a redução e eventual desaparecimento de uma bolha de recirculação a ter um grande efeito em termos de eficiência energética e na capacidade de direcionar as partículas para o filtro do exaustor, como desejado. Além disso, foi também estudada uma nova geometria já implementada no mesmo exaustor, de modo a avaliar o comportamento desta nova versão.

Foram realizados também testes experimentais, nos quais se verificou que um novo método para recolher os dados de perdas de pressão era consideravelmente melhor que o anteriormente utilizado. Também foi possível obter uma correlação entre os resultados numéricos e experimentais, com a proximidade dos valores a confirmar a qualidade dos estudos numéricos.

Palavras-chave: Exaustor perimetral, canal em ângulo recto, escoamento turbulento, deposição de gordura, CFD

Abstract

The following work focuses on the improvement of the channel geometry inside a perimetric exhaust, with the goal of improving the energetic and grease filtering performance. This is done via 2D numerical simulations, with an experimental part to assess the results obtained computationally.

The initial geometry was studied to act as an initial point of comparison to the first geometry variation, as well as to determine how different characteristics of the flow (recirculation zones) vary with different inlet velocities and working temperatures. Then, two first geometry variations were tested, both improving on the initial basis. The best one from those two went through another three iterations to maximize the improvement by reducing local pressure losses and grease depositing in the walls. All of the three new versions improved on the already upgraded geometry, with the reduction and eventual elimination of a recirculation zone having a great effect both in terms of energetic efficiency and also on the capacity to direct the grease particles to the filter, as desired. In addition, a new real geometry implemented in the same exhaust was studied and compared to the initial, in order to assess the behaviour of this new version.

An experimental test was also made, where a new method to collect pressure loss data was proved fruitful and a correlation was obtained between the experimental and numerical results, with the values being close enough to verify the quality of the numerical part.

Keywords: Perimetric exhaust, right-angled channel, turbulent flow, grease deposition, CFD

Contents

List of Tables

List of Figures

Nomenclature

Greek symbols

α_p	Coefficient of thermal expansion [1/K].
$\bar{\phi}$	Variable mean value.
ΔH	Enthalpy differential [J].
Δp	Pressure differential [Pa].
ϵ	Turbulent dissipation [m^2/s^3].
μ	Dynamic viscosity [Pa.s].
μ_f	Flow viscosity [Pa.s].
μ_p	Particle dynamic viscosity [Pa.s].
μ_t	Turbulent viscosity [Pa.s].
μ_τ	Friction velocity [Pa.s].
ν	Kinematic viscosity [m^2/s].
ω	Specific dissipation [1/s].
ϕ_i	Variable fluctuation.
ρ	Density [kg/m^3].
ρ_p	Particle density [kg/m^3].
σ_p	Particle surface tension [N/m].
τ_L	Lagrangian time scale.
τ_p	Particle response time.
τ_w	Wall shear stress [Pa].
ε	Wall roughness.
$\widetilde{\phi}$	Variable instant value.

Roman symbols

ω_{ij}	Mean rotation rate tensor.
$\widetilde{T}$	Favre temperature average [K].
A	Inlet entry section area [m].
C_D	Drag coefficient.
C_L	Lagrangian time scale coefficient.
C_p	Fluid specific heat capacity [J/(kgK)].
d	Pipe diameter [m].
D_0	Main reference dimension [m].
D_h	Hydraulic diameter [m].
D_p	Particle diameter [μm].
D_{ref}	Reference diameter [m].
f	Friction factor.
F_D	Drag force [N].
F_g	Gravity force [N].
F_L	Lift force [N].
F_{Tb}	Turbophoretic force [N].
F_{Th}	Thermophoretic force [N].
g	Gravity vector [m/s^2].
h	Convective heat transfer coefficient [W/(m^2K)].
h_1	Starting element size [mm].
h_i	Element size [mm].
h_m	Head loss [m].
I	Turbulent intensity.
K	Local pressure loss coefficient.
k	Thermal conductivity [W/(mK)].
k	Turbulent kinetic energy [J/kg].
k_p	Particle thermal conductivity [W/(mK)].

Kn	Knudsen number.
L	Pipe length [m].
m_p	Particle mass [kg].
P	Inlet entry section perimeter [m].
Pr	Prandtl number.
Pr_T	Turbulent Prandtl number.
Q	Additional heat sources [W].
q	Heat flux [W/m^2].
Q_p	Work done by pressure changes [W].
Q_v	Heat losses by viscous dissipation in the fluid [W].
Re	Reynolds number.
Re_p	Particle's relative Reynolds number.
S_{ij}	Mean strain rate tensor.
St	Stokes number.
T	Fluid temperature [K].
t	Time [s].
U	Inlet velocity [m/s].
u	Fluid velocity [m/s].
U_0	Flow velocity [m/s].
U_{ref}	Reference velocity [m/s].
v	Particle velocity [m/s].
V_m	Cross section's mean velocity [m/s].
V_{max}	Maximum inlet velocity [m/s].
V_{min}	Minimum inlet velocity [m/s].
y^+	Non-dimensional wall distance [mm].

List of Abbreviations

DNS	Direct Numerical Simulation. 14, 15
IAQ	Indoor Air Quality. 2
LES	Large Eddy Simulation. 15
PDE	Partial Differential Equation. 20
PIV	Particle Image Velocimetry. 27, 28, 54
PLA	Poly-Lactic Acid. 26, 27, 29
RANS	Reynolds-Averaged Navier-Stokes. 15
RSM	Reynolds Stress Model. 15
SST	Shear Stress Transport. 16

Chapter 1

Introduction

1.1 Motivation

The importance of environmental measures has been increasing in the past few years. With climate change becoming more real each year that goes by, energetic improvements are discussed and made in every single possible way. Household appliances are no exception to it, including kitchen exhausts.

Kitchen exhausts perform a very important task as they clean up the air during cooking tasks, helping to avoid spreading air polluted with water vapours, grease particles and others (including odors) in its vicinity, while avoiding also a temperature rise in the room from those activities. Perimetric exhausts perform just that while keeping all grease particles captured in the operation stored in a zone further away from the surrounding air, allowing a cleaner environment in the kitchen and giving it a fresh, modern look.

Both points, energetic consumption and grease filter efficiency, are between the 4 classes evaluated and classified by a set of rules created by the European Commission. Those regulations, Nº65/2014 [1] and Nº66/2014 [2], are in effect for kitchen exhausts since January 2015. They also oblige the exhaust to go through several standard tests with a final overall grade being awarded as a result of the combined efficiency scores once all measurements and calculations are completed.

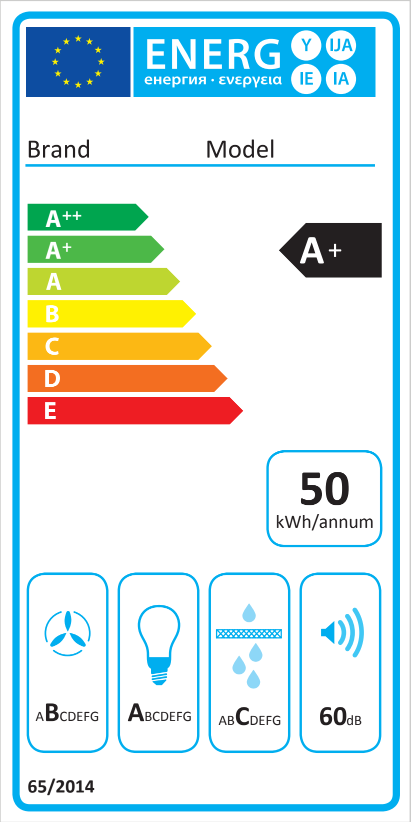

Figure 1.1: Example of a label in a kitchen exhaust for sale in 2019.

That grade can go from A+++ (most efficient) to G (less efficient), although only 7 of these 10 will appear on the label: in January 2015, when the regulation was first released, the grading went from A to G. Since January 2018, labels follow the format of the one represented in Figure 1.1, graded from

A++ to E, and from January 2020 onwards it is mandatory for the grading to be presented from A+++ to D.

This represents more demanding standards to be released soon and, as such, a decrease in classification for companies that do not upgrade the performance of their kitchen exhausts, leading even to a prohibition to sell some of the less efficient products. It also represents an opportunity for companies to be up to the state of art and sell their products as the best in the market. Moreover, it is a chance for house-owners to purchase a more environmental friendly device and, at the same time, reduce the cost of their electricity bills considerably.

For this reason, the optimization of perimetric exhausts is of great interest for both industry and its costumers. Hence, this work will focus on maximizing its energetic performance for the same initial input and improving the grease particle behaviour.

1.2 Theoretical Overview

This thesis focuses on the specific behaviour of perimetric exhausts, both in terms of the flow dynamics and the particles it contains. This type of exhausts are characterized by not having the filters right next to the air intake, in direct contact with the kitchen environment. Instead, the air is directed through a small gap that goes all around the extremity of the exhaust, being diverted inside to its centre, where the filter is, as it is show in Figure 1.2.

Figure 1.2: Cross-section representation of a perimetric exhaust (adapted from [3]).

While this has the advantage of improving the Indoor Air Quality (IAQ) of the room, it comes with disadvantages. The deflection imposed to the flow in the channels by the 90 degree angle after the entrance implies a loss of energy before reaching the fan that other exhausts do not have, turning it into a less efficient and more energy consuming exhaust. In addition, the tightness of the channel and its corner may imply that not all of the particles contained in the flow pulled by the fan reach the filter, as desired. In a worst case scenario, this might result in some grease slipping to the entry gap and even dripping to the exterior.

This work follows the studies made by both Ferro [4] and Monteiro [5], and will simplify the geometry of a perimetric exhaust to a bi-dimensional channel representing one of the sides of the exhaust, in order to obtain reliable results in a less computationally expensive way during numerical studies, and throughout a simpler bi-dimensional equivalent representation during experimental studies that will allow to understand the basic behaviours of the flow without requiring a full exhaust setup and extremely complex methods.

1.2.1 Exhaust channels

The inlet channels, narrow and with sharp-edge corners inside, are the cause for the complexity of this problem. A narrow entrance allows for considerable inlet velocities. Following the measured values in [4] and using the definition for hydrodynamic diameter according to [6], the Reynolds number values obtained are always either in the turbulent region, or in a near-turbulent transition zone. The sharp edges presented to the flow, originally in a form of a 90 degree angle, would always result in its transition to turbulent, even if the entry values are lower, just as seen in [5]. Therefore, the flow throughout this work was considered to be fully turbulent, adding more complexity to the numerical part of the flow study.

The sharp angles present in the geometries of this work create large pressure gradients after the corner, which results in flow separation and therefore a loss of energy from the flow. A separated flow means the appearance of recirculation bubbles where exists a free shear layer, naturally unstable, which could, to an extent, cause damage to the exhaust [7] via fatigue forces applied in the thin exhaust metal plate. This could be made worse by having a turbulent flow, where mass transfer rates and entrainment are increased compared to a laminar regime [8], which leads to an increase on the variation of the load intensity.

Without being able to change the entrance area or shape, in order to keep the same flow rate and suction capacity from the exhaust and avoiding any new molds for its manufacturing, this work will apply simple geometric changes to the sharp-edged zone in order to mitigate the effects verified in previous studies, quantifying the improvements made in the exhaust's performance. This will be done by designing new geometries, still maintaining corners due to the company's necessity for simple manufacturing, but with reduced angles.

1.2.2 Pressure losses throughout the exhaust

Due to its shape, the exhaust channels can be related to a piping system, more specifically a non-circular duct. Although in more regular, grid exhaust systems, the losses are mainly located in the fan [9], the existence of a complex interior geometry in a perimetric exhaust makes it the main point of study before turning attention to the fan area.

According to [6], the losses in a pipe flow can be divided into two types: friction losses and local losses. Friction losses result from shear stresses applied to the flow in line sections of the duct, where the flow is fully developed, causing it to lose energy. In this work, however, local losses are the main topic since that is how most of the energy is removed from the flow. They refer to, as the name says, local effects created due to any kind of disturbance to the natural track of the flow, as, for example, valves, entrances/exits, any sudden area variations or, what's present in this case, bends.

To evaluate local losses in duct flows and compare similar cases, it is used a dimensionless value: the local pressure loss coefficient, K. The value of the coefficient for a certain case reflects how big the pressure loss is in the corresponding zone of analysis. A higher value of K corresponds to a bigger energy loss. Table 1.1 presents some values of K. Note how a tighter corner relates to a bigger value for K, as the flow loses more energy with the increase of the pressure gradient and bigger possibility to form recirculation zones during the corner.

Table 1.1: Example of values for K in a circular section flanged pipe with elbows of different angles (adapted from [6]).

Pipe nominal diameter [mm]	25.4	50.8	101.6	203.2
45° long radius	0.21	0.20	0.19	0.16
90° long radius	0.40	0.30	0.19	0.15
180° long radius	0.40	0.30	0.21	0.15

A more theoretical definition, shown in Equation 2.7 is given in [6], where it's defined as the ratio between the head loss in the zone, h_m, and the velocity head of the system, $V^2/(2g)$.
$\Delta p = p_1 - p_2$ represents the local pressure drop in the pipe (in this study, between the entrance of the channel and the point where the flow resumes to be fully developed), ρ the density of the fluid running in the pipe and V_m the cross-section's mean velocity at the entry section, the same section in which p_1 is taken. Figure 1.3 below displays a schematic showing an example of how K is measured in this work, with point 2 being located 60 mm after the inside point of the corner.

$$K = \frac{h_m}{\frac{{V_m}^2}{2g}} = \frac{\Delta p}{\frac{1}{2}\rho {V_m}^2} \tag{1.1}$$

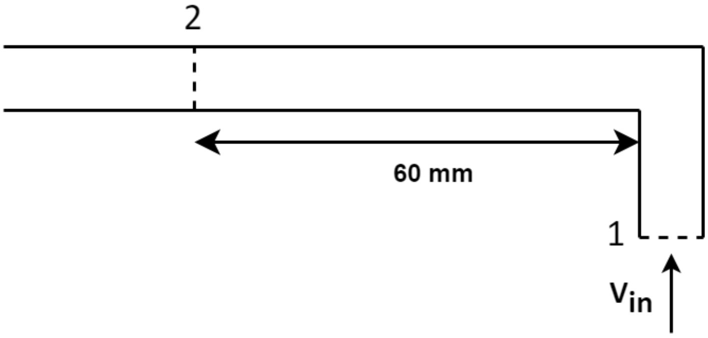

Figure 1.3: Schematic of a data measurement to retrieve a value for K.

Although it's not the main focus on this work, friction losses still exist in a real flow inside a perimetric exhaust. For a case where several local losses occur in different ways or zones, Equation 1.2 represents the total sum of losses along the pipe system, where f stands for the friction factor, L the length of the pipe and d the diameter of the pipe.

$$\Delta h_{total} = \frac{V^2}{2g}\left(\frac{fL}{d} + \sum K\right) \tag{1.2}$$

The first term of the sum in Equation 1.2 refers to the friction losses in the pipe and can only be used assuming the flow is in a fully developed zone, where the pressure decreases linearly along the length of the tube and the wall shear stress, τ_w, is constant [6]. Despite being most times less significant than the local losses, the influence of the first term can be determined by the value of the friction factor f, which depends on the value of the flow's Reynolds number, Re, and on the wall roughness, ε. If the pipe walls have a high ε, then f will be constant for high Re. On the other hand, if ε is low then the walls are considered *hydraulically smooth*, which means that the wall roughness will not affect the friction value and, therefore, the first term in the Equation 1.2 can be neglected. After obtaining those values, the value for f can be determined by using the Moody chart [6].

Although the heat from the stove is supposed to be transferred to the food being cooked, some losses end up occurring in the system during the activity. Food releases heat through the air and water vapour, which ends up being extracted by the exhaust. This means that, in reality, the exhaust is not going to be operated at room temperature but considerably above it. Therefore, some heat transfer may occur from the air to the steel plates that make the surface of the channels. It also means that some of the flow properties are going to be affected. Density, ρ, and dynamic viscosity, μ, for example, vary with temperature. Knowing that the Reynolds number depends on both properties plus the reference velocity U_{ref} and diameter D_{ref}, as it is described in Equation 1.3 below, this means that the Reynolds number at the inlet of the exhaust will not only depend on the power selected from the user to the exhaust (and therefore, the inlet velocity), but also from the working temperature at the entry of the exhaust, with density having a larger variation and, therefore, larger influence in that parameter.

$$Re = \frac{\rho U_{\mathrm{ref}} D_{\mathrm{ref}}}{\mu} \tag{1.3}$$

For this reason, studying how the temperature affects the flow parameters and characteristics inside the channel is also important to the present work.

1.2.3 Two-phase flow

The flow inside an exhaust has a distinguished complexity not only because of the channel geometries perimetric exhausts have, but also because the non-isothermal flow inside is not just purely air. As it was mentioned before, it also includes a mix from the cooking activities performed underneath the exhaust, mainly composed by water vapour and grease particles [10]. The small size and mass of these particles contributes to an increase in difficulty when attempting to study their behaviour, specially taking into account the randomness produced by both the cooking process and the turbulence in the flow.

The mass changes from particle to particle, enough to affect their movement and thus, the amount of deposition in the walls [11]. Their behaviour can be characterized by the dimensionless Stokes number, St, presented in Equation 1.4, a ratio between the particle response time, τ_{p}, or relaxation time of the particle (the time a particle needs to be in equilibrium with the flow after being affected by a force) and the residence time of the particle in that said flow or Lagrangian time scale, τ_{L}. It depends on the particle density, ρ_p, its diameter, D_p, the viscosity of the flow, μ_f, the main reference dimension, D_0 and the flow velocity, U_0.

$$St = \frac{\rho_p {D_p}^2/18\mu_f}{D_0/U_0} = \frac{\tau_\mathrm{P}}{\tau_\mathrm{L}} \tag{1.4}$$

A smaller Stokes number is then, by definition, representing a small particle, and bigger or heavier particles have a bigger Stokes number. According to [12], particles with a lower relaxation time, that is, St considerably under 1, spend less computational time because they enter easily in an equilibrium state. For that same reason, they have a bigger tendency to follow the streamlines from the flow they are in. On the other side, a bigger Stokes number ($St > 1$) means they can leave recirculation zones and vortexes due to their inertia [13].

Drag force is the dominant aspect for particle movement when the particle density is considerably bigger compared to the fluid flow's density [13]. [14] also states that for particle diameters bigger than 0.1 micrometers, gravity forces should not be discarded when studying particle deposition. But other phenomena can also have an effect on particle movement. For example, particles in turbulent flows can be affected by turbophoresis, a tendency for the particles to move in the direction of zones with minor turbulence levels. Due to big variations in the values for vertical velocities near walls, this effect may impose an increase of particle depositing in the walls surrounding the flow [15, 16], particularly in the case being studied since this effect can be amplified for the particle diameters being studied [17].

The flow temperature also affects the particles in other ways beyond affecting the flow, bringing more effects to influence the particle movement. Thermophoresis, for instance, adds another complexity point to the flow. This phenomena appears with the existence of thermal gradients, causing particles with higher temperature, and therefore more energy, to transform it into kinetic energy: velocity. This may cause particles from zones with higher temperature to relocate to zones with a lower temperature via thermophoretic forces, in order to achieve equilibrium. This effect has been used as a way to avoid particle seeding in walls by heating them up [18] but, on the contrary, in the case of flows with near cold walls, this might convert in even more particle depositing. For a turbulent thermal boundary layer, a wall-flow temperature difference of around 30°C is already considered significant [19]. It's also known that a non-fully developed flow (thermally and hydrodynamically) may reduce that temperature difference, since a bigger mixture in the flow results in a smaller discrepancy in temperature [20].

For near wall flows including particles, the effect of lift forces should also be evaluated. They're created due to strong velocity gradients near the walls, pushing the particles away and avoiding their contact with the wall in certain conditions. For a laminar Poiseuille flow, due to the nature of its parabolic velocity profile, it means that the particles will merge to a near-wall region [21]. That means that the boundary layer and all of the flow near-wall must be studied carefully to make sure the wall deposition is accurately modelled.

Two different routes can be taken when studying a two-phase flow numerically. The options available are either a Eulerian or a Lagrangian approach. The Eulerian method sees the particles as a continuum phase and calculates the equations affecting their movement in fixed control volume, similarly to the calculations to the fluid flow. The Lagrangian method however, sees the particles as a discrete phase inserted in the continuum fluid phase, where the equations are applied individually to each particle to represent the different forces acting on them. This means that the Lagrangian method is more influenced by the fluid flow's accuracy [22], requiring it to be well modelled in order not to affect the precision for the particle tracing studies.

Both have been used in separate previous studies about particle deposition and movement in fluid flows: for the case of Eulerian methods, [23] measures particle deposition in a chamber and [14] studies particle deposition in an indoor surface from a turbulent flow, analyzing it separately in each zone. With a Lagrangian approach, there are several cases: [24] studies the concentration of oil particles in a kitchen with a numerical part with the Lagrangian method. There are also papers comparing both approaches for similar cases [13, 25] in order to better understand each of their advantages, with the Lagrangian method being the preferred for unsteady conditions, although they state that none of the methods is clearly superior to the other.

Despite being difficult to model the real case numerically in a correct and accurate way due to the factors mentioned in the last paragraphs, experimental studies are often impractical to perform due to the small, variable size of the particles and the inability to accelerate the processes to obtain faster data for deposition values. Retrieving such values accurately is difficult and the randomness in the flow referred to before can also influence the results in an experimental test, making it near impossible to obtain consistent results and draw conclusions [22].

The following work takes on the numerical studies with a Lagrangian method as a follow-up from the previous study [5] but also because it better characterizes the particle depositing as an individual study, allowing to perform fluid flow and particle tracing simulations individually and in a more efficient way.

1.3 Objective

This work has the objective of improving the energetic performance of the perimetric exhaust being studied, while controlling and trying to direct the grease particles contained in the flow to the desired location: the filters, avoiding its deposition in the exhaust's walls.

The numerical part of this work will be performed using the commercial software *COMSOL MULTIPHYSICS®*, a multi-physics software that allows to perform flow simulations but also integrate particles in the flow in order to execute separate particle simulations with the basis from the previously done flow simulation files. This allows not only to analyse several parameters from the flow inside the channels in order to check its energetic performance, but also to replicate the movement from these particles contained within the flow to check where are their deposition points and the amount or percentage of particles that actually end up in the filters, as it is preferred.

It was also conducted some experimental tests in order to assess the quality of the numerical results obtained through an acrylic prototype from a previous study, which was refined and adapted to a new geometry.

1.4 Thesis Outline

This thesis is divided in 4 chapters. The present chapter, Chapter 1, serves as an introduction to the topic, delivering an insight to the work to follow, the motivation behind it and explaining some phenomena that affects the study by discussing some papers related to the subject.

Chapter 2 takes on the procedures carried out in this work, both in the numerical and experimental parts. It introduces the exhaust and how it was studied, including the simplifications made to it; the program in which the numerical simulations are run, the options undertaken when facing up with decisions and the hurdles faced along the way. It also presents the experimental set-up and the simplifications made to allow direct comparisons between the experimental and numerical parts, and the real case.

Chapter 3 presents the results from both the numerical and experimental cases, with an analysis to the individual numerical case studies and a comparison between them, allowing to see the main differences and improvements from the different geometries, followed by the experimental part which brings an evaluation of the quality of the numerical case.

Finally, Chapter 4 finishes by providing some conclusions from the work done and delivers a proposal of future work, in order to provide directions to continue this study.

Chapter 2

Methodology, Computational Overview and Experimental Setup

The thesis focuses on studying the two-phase flow inside the channels of the exhaust and how to improve its performance by optimizing their geometry. For that, numerical simulations, following up to the work of Monteiro [5], were carried out changing several parameters in order to analyse how it affects the pressure losses and particle deposition. An experimental setup was adapted from the work of Ferro [4] to assess the results obtained numerically.

2.1 Exhaust Overview

The exhaust analysed in this study is a perimetric exhaust. This type of exhausts are characterized by an entry slot that goes all around the near-edge of its inferior surface, as it was previously shown in Figure 1.2, giving access to the channels being studied. The exhaust has 3 different working powers for the consumer to use (P_1, P_2, P_3, lower to higher), which correspond to three different air mass flows being extracted by the exhaust (234 m^3/h corresponding to the lowest power to 380 m^3/h for the highest power) and therefore, three inlet velocities, V_1, V_2 and V_3. The real exhaust has the following dimensions: 900 mm of length, 480 mm of width, 700 mm of height. The exhaust pipe, carrying the exhaust's electric fan, has 330 mm of length and 270 mm of width and it is slightly off center to the rear. However, despite knowing from [4] that this ends up affecting slightly the flow symmetry along the exhaust, this is disregarded in this work for the sake of simplification.

To study the flow inside the channels, a 3D representation would be more realistic than a 2D representation. However, to recreate that numerically would require a huge computational demand, and to visualize the flow inside the channels experimentally it would be necessary to build an enormous apparatus. Therefore, the most logical solution is to simplify and study only a 2D cross-section of the exhaust's channel which will still give representative numbers for the local losses and predict the particle deposition in the channels.

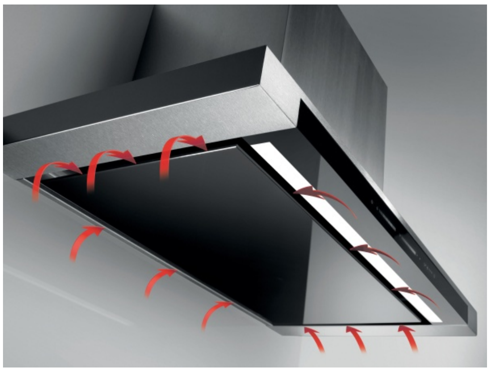

Figure 2.1: Representation of a perimetric exhaust (extracted from [5]).

2.2 Software and Numerical Simulation Overview

The 2D representation of the unit shown in Figure 2.1 was studied numerically in a multiphysics commercial software: *COMSOL MULTIPHYSICS®*. The use of this software allows to simulate several physics in different studies, some at the same time. Since this case covers several types of studies (heat transfer, fluid dynamics and particle tracing), this makes it the ideal program to run the studies related to this work. The program is installed in a computer with the following characteristics: 2 processors of 2.40 *GHz* and 48 *Gb* of RAM, with a *Windows 10* software.

The numerical simulations focus mainly on the corner of the exhaust's channel. That is the zone where the predominant losses inside the channel occur: the local losses. For this reason, the geometries that will be studied will have their inlet at the entry of the channel, and their outlet far enough so that pressure can be assumed constant at the outlet, with the flow in a fully developed state.

2.2.1 Geometries

Several different geometries were put into test to verify how they were impacted by different velocities and by changes in the flow temperature. Ergo, code names were created in order to easily identify each of the different geometries. It was also created a color scheme for an easier recognition of each boundaries: green was assigned to the inlet, red to the outlet and black to the remaining walls.

Firstly, the study begins with geometry A. This geometry, represented in Figure 2.2, is the equivalent to the real initial geometry of the exhaust, analysed in the studies that preceded this work [4, 5]. It is formed by 3 rectangular shapes, characterized by a constant thickness of 10 mm, with an entry zone with 20 mm of length and a straight exit zone with 100 mm.

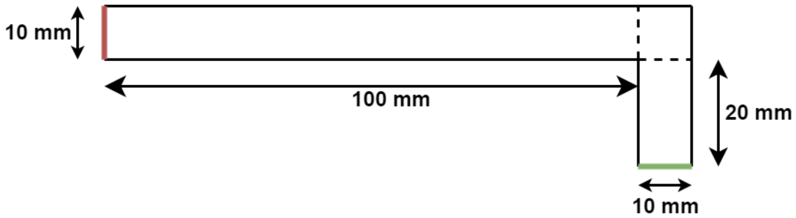

Figure 2.2: Representation of geometry A.

Two new geometries followed as a starting point for the geometry improvement of the channel: geometries B and C, respectively. Both geometries represent a small change to the initial one (geometry A), allowing them to be produced without big changes to the manufacturing process, as desired by the company that produces these perimetric exhausts.

Geometry B (Figure 2.3) is almost an identical copy of geometry A, with the same inlet and outlet of 10 mm, but with one subtle change: the point to the inside of the 90 degree angle is moved from its original position 10 mm to the left. This transforms the exit zone into a rectangle with 90 mm of length and 10 mm of width and the entry zone into a trapezoid with 20 mm of height, 10 mm at the bottom and 20 mm at the top, reducing the angle of the corner in which the flow will go by. Although it might create a bigger recirculation zone in the top right corner, it should reduce the recirculation zone near the bottom wall, after the corner.

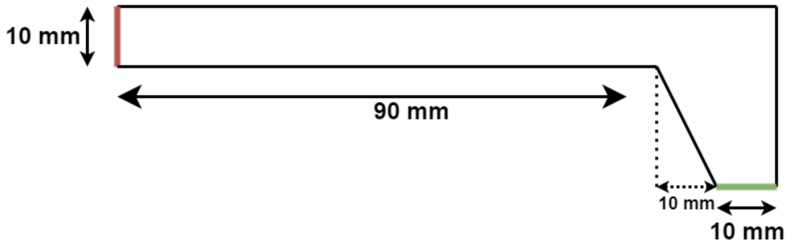

Figure 2.3: Representation of geometry B.

Geometry C (Figure 2.4) is a slightly more complex version of the initial geometry, as it replaces both the inside and outside points in the 90 degree corner for two diagonals that make a 45 degree angle with both the entry and exit zones. This way, the exit zone's length is reduced to 95 mm and the entry zone's length to 15 mm, keeping the same thickness of 10 mm at the inlet and outlet. This represents an attempt to create a smooth corner but instead of rounding the metal plate making the inside wall of the channel, which would require new molds to produce the exhaust, it is bent in two consecutive points. This adapts more to the natural movement of a flow and should reduce the recirculation areas all around the zone.

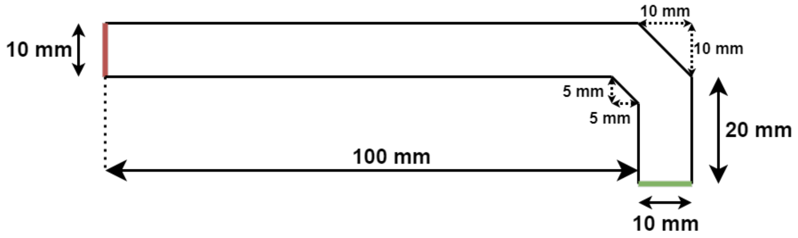

Figure 2.4: Representation of geometry C.

In the following step of the optimization process, three more geometries were created. For reasons later explained, these three geometries are variations from geometry B: geometries B15, B20 and B30. The codes names reflect their characteristics: B tells that the following geometry is a different version based on geometry B, and the number represents the distance in which the inside corner point was moved to the left, from its original spot, represented in Figure 2.5 by the measurement x. Therefore, only the top entry zone and exit zone length change from geometry B, keeping a trapezoid with the same entry lengths of 20 mm for the height and 10 mm at the bottom. The variable values are given in Table 2.1.

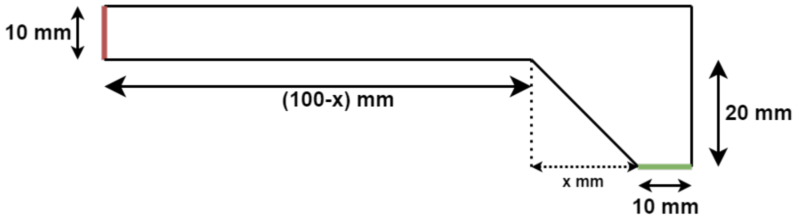

Figure 2.5: Representation of the optimized geometries Bx.

Table 2.1: Variable size values for geometries B15, B20 and B30.

Geometry Bx	Entry Zone top length	Exit Zone length
B15	25	85
B20	30	80
B30	40	70

Recently, some adjustments in the exhaust's manufacturing led to a considerable change in the channel geometry. Hence, it was decided to run new studies with the most recent geometry to see how it affects the particle deposition and the pressure losses in the exhaust system. The new geometry, named geometry D, represents an increase in area to geometry A, with a decrease in half for the height of its entry zone. From the outlet line, it is added underneath the exit zone two new areas, increasing the outlet length to 19 mm. The L shaped empty zone in the middle of the geometry represents the continuation of that metal plate to the inside of the exhaust, separating the entry zone to the rest. For reasons later clarified (see Chapter 3.2.1), it was also created a second geometry, geometry E, equal to geometry D but with the outlet further 150 mm away from the outlet of geometry D, extending the exit area to a length of 250 mm. Both geometries are represented below in Figure 2.6.

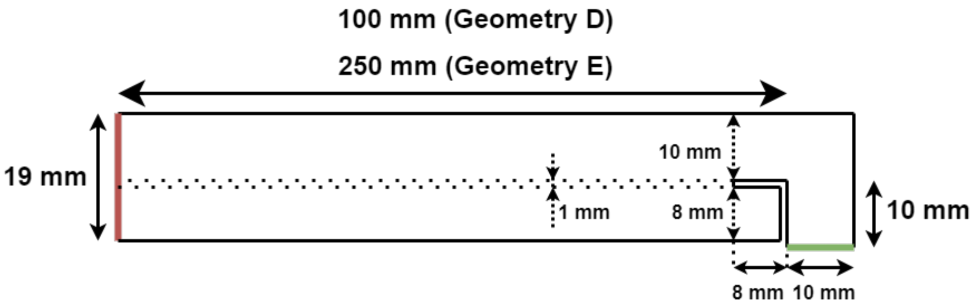

Figure 2.6: Representation of geometries D and E.

The last geometries studied were an alternative of geometry E but with the outlet 50 mm closer to the entry zone, since the flow will become fully developed faster and a shorter geometry means less calculation in the simulation, using less computational time. Geometries E10, E15, E20 and E30 follow the same logic from geometries B, B15, B20 and B30, where the metal plate on the left of the entry zone was bent in a way that moves the point on the inside of the 90 degree corner by 10, 15, 20 or 30 mm to the left, respectively. That value is represented in Figure 2.7 by the measurement x. This is intended to produce the same effect as in geometry B, reducing the angle the flow has to face and with that, hopefully, reducing the pressure losses.

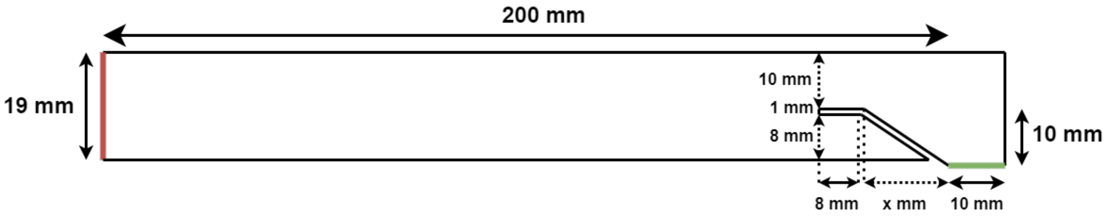

Figure 2.7: Representation of the optimized geometries Ex.

2.2.2 Numerical studies

For all geometries referred to before, numerical studies were conducted to determine the local pressure losses and study the particle movement and deposition and also how the different inlet velocities and temperatures would change the characteristics and final results. The two points to be studied, the flow and particle analysis, were performed separately. Firstly, the fluid flow simulations were run, allowing any unexpected difficulties, tuning necessary to the simulation parameters or errors to be detected in less time, since a simulation with all the physics together would increase considerably the computational running time, and that any wasted time in simulations with mistakes in it would be minimized. Thus, the particle simulations began only after each geometry's flow simulations were successfully completed and analysed.

Due to the nature of the flow simulation, which includes a heat transfer module to reproduce the effects of the heated air inside the channels of the exhaust in order to include the effect of temperature, the simulations were made with compressible flow, specifically with the weakly compressible flow physics. This option includes the same equations as the compressible flow physics but assumes the density values at reference pressure, that is, in this case, at atmospheric pressure [26]. Since this does not change the values considerably and allows for the computational time to go down, this option was preferred to the regular low-velocity compressible flow physics. The density and dynamic viscosity values used in this study are presented below in Table 2.2 for each of the studied temperatures.

Table 2.2: Values from *COMSOL* for density, ρ, and dynamic viscosity, μ, at atmospheric pressure.

T [^{o}C]	10	20	30	40	50	60	70	80	90	100
ρ [kg/m^3]	1.2469	1.2044	1.1646	1.1275	1.0926	1.0598	1.0289	0.9998	0.9722	0.9462
μ [10^{-5} Pa.s]	1.7642	1.8140	1.8629	1.9110	1.9584	2.0050	2.0508	2.0959	2.1402	2.1839

Fluid flow simulations

The fluid flow numerical simulations were solved in *COMSOL MULTIPHYSICS®*, performed by a steady-state solver. Therefore, all time dependent terms (Equation 2.1) will be eliminated from the calculations of the model equations to be presented throughout this section.

$$\frac{\partial}{\partial t} = 0 \tag{2.1}$$

As seen in the previous work from Monteiro [5], the flow inside the channel was proven to be in turbulent conditions for ambient conditions, contrary to what was originally thought. However, in this work, the values for Reynolds number are calculated using the definition of hydraulic diameter, since the cross-section of the channels are not circular. As it is seen in Equation 2.2, where it is proved for a generic long rectangular inlet ($h \ll b$), with height h and width b tending to infinity (being A the entry section area and P the entry section perimeter), the hydraulic diameter D_h is twice the value for the original diameter. So, the Reynolds number was calculated with a value of D_h = 20 mm based on the value of h = 10 mm from the geometry inlet. The range for transition and turbulent in pipe flows is still discussed and not fixed in a value.

$$D_{\mathrm{h}} = 4\frac{A}{P} = \frac{4h}{2(h/b+1)} \xrightarrow{b\to\infty} 2h \tag{2.2}$$

Although the most common Reynolds value for transition in circular pipes is around 2300 [6], other papers in different conditions refer lower values. A study on particles in channels with a flow in transition regime [21] says that the transition regime begins for Reynolds values over 1575 and ends at 2000. Even the own channel geometry can force transition, since the corner or even the channel entry can bring disturbances to the flow, ceasing any doubts that the range of Reynolds numbers could create. By verifying the Reynolds number values for each of the studied velocities and temperatures, as seen below in Table 2.3, it is shown that all values are still in the range suggested above, specially with higher inlet velocities or temperatures lower and closer to the normal ambient temperature.

Table 2.3: Values of Reynolds for all inlet velocities and temperatures studied.

T [ºC]		10	20	30	40	50	60	70	80	90	100
U = 2,02	[m/s]	2855	2682	2526	2384	2254	2135	2027	1927	1835	1750
U = 2,08	[m/s]	2940	2762	2601	2454	2321	2199	2087	1984	1890	1802
U = 2,21	[m/s]	3124	2935	2763	2608	2466	2336	2218	2108	2008	1915
U = 2,37	[m/s]	3350	3147	2963	2797	2644	2505	2378	2261	2153	2054

After acknowledging that the flow to be studied was turbulent, a mathematical model was chosen in order to solve the problem. Being a highly complex type of flow, with 3D effects, high diffusivity, unsteady and very unpredictable due to its aleatory nature, a turbulent flow (and turbulence itself) is very difficult to recreate accurately in numerical studies [8]. The most accurate model available to this date would be the Direct Numerical Simulation (DNS), which allows to calculate the fluid flow 3D effects and both bigger and smaller eddies in a transient condition due to its small spacial grid and time-step.

However, the cost of such accuracy is a huge computational demand, resulting in a very high computation time. Large Eddy Simulation (LES) is similar to DNS but, as the names says, calculates only the large scale eddies. This implies extra models for studies with near-wall and/or particle simulations. Filtering the smaller eddies allows for a reduction in computational time compared to DNS but the calculations are still very heavy and time consuming, being both normally (but not always, as seen before in [19]) disregarded from most studies for that reason. Therefore, the transient part of the simulation is what costs more time to the study [8].

Making the study steady-state and averaging the properties of the flow saves a lot of calculations necessary in the previously referred to models and, consequently, reduces the computational time. This is done by the Reynolds-Averaged Navier-Stokes (RANS) model, which, as it says in the name, makes a statistical time average to the dependent variables of the Navier-Stokes equations. This is known as the Reynolds decomposition method, represented in Equation 2.3, where $\widetilde{\phi}$ represents any variable in a certain instant, $\bar{\phi}$ is the mean value of the same variable and ϕ_{i} the fluctuation value of the variable, to the mean value, in that same time instant. This method allows RANS to be much lighter computationally compared to DNS and LES, which is why this model is the most used in engineering and practical cases and also why it is the one chosen to be used in this work.

$$\widetilde{\phi} = \bar{\phi}_{\mathrm{i}} + \phi_{\mathrm{i}} \tag{2.3}$$

Since the compressibility element is present in the cases under analysis, the Navier-Stokes equations (Equation 2.4) are composed of two balance equations to be calculated by the solver: the mass balance equation (Equation 2.4a, also known as the continuity equation) and the momentum balance equation (Equation 2.4b), plus the the energy equation (Equation 2.4c).

$$\nabla(\rho\bar{U}) = 0, \tag{2.4a}$$

$$\rho\bar{U}\nabla\bar{U} = -\nabla p + \nabla\Big((\mu+\mu_T)(\nabla\bar{U} + (\nabla\bar{U})^{\mathrm{T}}) - \frac{2}{3}(\mu+\mu_T)(\nabla\cdot\bar{U})\Big) + F \tag{2.4b}$$

$$\nabla(\rho\bar{U}\bar{E}) = -\bar{p}\nabla\bar{U} - \nabla\big(q + q^T\big) + \nabla(\bar{U}(\mu+\mu_T)\Big(\nabla\bar{U} - \frac{2}{3}\nabla\cdot\bar{U}\Big) + Q \tag{2.4c}$$

This set of equations are formulated already taking into account the simplifications made in a steady-state form, using the variables in its averaged form due to the use of RANS in the work and including a turbulence model, which is required to solve the unknowns in the equations above. This will solve the Reynolds stresses, $\rho(\overline{u \times v})$. There is a wide array of possibilities to start: the Reynolds Stress Models (RSM) solve the equations directly for $\rho(\overline{u \times v})$ with 6 extra transport equations. The more commonly used Eddy-viscosity models solve the equations for the turbulent (or Eddy) viscosity, μ_{t}. They are based on the Boussinesq approximation, expressed in Equation 2.5, known as the Reynolds stress transport equation, where k is the turbulent kinetic energy, which states that the Reynolds stresses are proportional to the mean velocity derivatives, with the proportionality factor being the Eddy viscosity.

$$\rho(\overline{u \times v}) = -\mu_t(\nabla\bar{U} + (\nabla\bar{U})^{\mathrm{T}} - \frac{2}{3}\nabla \cdot \bar{U}) - \frac{2}{3}\rho k \tag{2.5}$$

This is a way of representing the Eddy viscosity as the responsible for momentum transfer and, therefore, represent in increase in turbulence as an increase of viscosity [27]. There exists several types of Eddy-viscosity models as well, such as Algebraic models or 1-equation models. However, the 2-equation models are the most common of all these, as they add some complexity and accuracy without much computational cost. That complexity comes with the increase to two extra equations to solve μ_{t}, completing the system with more knowledge about the flow variables, including information about its energy and diffusion effects, for example. One of the most used is the k-ϵ model, which provides information about the turbulent kinetic energy, k, and the turbulent dissipation, ϵ. However, this model can not be applied next to the wall without any extra development models and does not take into account turbulent anisotropy, like most 2-equation models [16, 28]. It also gives bad results when facing unfavourable pressure gradients, making it a bad choice for this work.

Others models include the k-ω and k-ω SST. The latter one is a version of the first that combines the good behaviour of the k-ω model in near-wall conditions with the k-ϵ results in free-stream flow. However, due to its simplicity, the adaptability to the case in study and following the work of Monteiro [5], the chosen model was k-ω. This model is capable to make correct calculations even into the boundary layer zone and although it might give problems with incorrect values for transition, that should not be a problem in this work since the entry of the channel and the corner forces the transition to happen even for lower values of Reynolds than expected. This 2-equation model, one of the oldest and most popular, provides information about the turbulent kinetic energy, k, and the specific dissipation, ω, solving the Eddy viscosity through Equation 2.6.

$$\mu_t = \rho\frac{k}{\omega} \tag{2.6}$$

The equations for the calculation of both k and ω are provided from *COMSOL* and expressed below, in Equations 2.7 and 2.8.

$$\frac{\partial\rho k}{\partial t} + \bar{U}\nabla(\rho k) = P_k\nabla\bar{U} - \rho\beta^* k\omega + \nabla((\mu + \sigma^*\mu_T)\nabla k) \tag{2.7}$$

$$\frac{\partial\rho\omega}{\partial t} + \bar{U}\nabla(\rho\omega) = \alpha\frac{\omega}{k}P_k\nabla\bar{U} - \rho\beta\omega^2 + \nabla((\mu + \sigma\mu_T)\nabla\omega) \tag{2.8}$$

where P_k is defined by:

$$P_k = \mu_T(\nabla\bar{U} \cdot (\nabla\bar{U} + (\nabla\bar{U})^{\mathrm{T}}) - \frac{2}{3}(\nabla\bar{U})^2) - \frac{2}{3}\rho k\nabla\bar{U} \tag{2.9}$$

The values for the parameters used in the previous equations are the same from the work of Monteiro [5], which follows the values advised by the *COMSOL* User Guide [29] for this model: α=13/25, β_{0}=13/25, β_0^*=9/100, σ=1/2, σ^*=1/2, with $\beta_0 = \frac{\beta}{f_\beta}$, $\beta_0^* = \frac{\beta^*}{f_\beta}$, $f_\beta = \frac{1+70\chi_\omega}{1+80\chi_\omega}$ and $\chi_\omega = \frac{\omega_{ij}\omega_{jk}S_{ki}}{(\beta_0^*\omega)^3}$, where ω_{ij} is the mean vorticity rate tensor and S_{ij} is the mean strain rate tensor. For the inlet conditions, the value of k for the different simulations was taken from the definition of isotropic turbulence [30], expressed in Equation 2.10, where U is the inlet velocity and I is the turbulent intensity (Equation 2.11).

$$k = 1.5I^2U^2 \tag{2.10}$$

$$I = \frac{u}{\overline{U}} \tag{2.11}$$

Typical values for the turbulence intensity go from 0.01 to 0.1 and, although some tests were performed to see how it affected the flow, those were rather inconclusive. So, the decision was made to stick to the value used by Monteiro [5] of 0.055. The initial conditions for the specific dissipation (ω) followed also the same procedure from [5], using Equation 2.6 with an initial value of ν_t=0.02.

At the wall boundaries, two conditions were set for the fluid flow module: since they are recreating the solid metal walls of the exhaust channels, an impermeability condition had to be set, meaning that no flow could go beyond those walls. The second one, since the simulation is for a viscous flow, was the no-slip condition. This means that the flow in direct contact with the wall must have the same velocity as the wall, which in this case, since it is not a moving wall, must be represented the following way, where y is the perpendicular distance to the wall:

$$U \mid_{y=0} = 0 \tag{2.12}$$

The wall shear stress, τ_w, is calculated through the following formula:

$$\tau_w = \mu \frac{\partial U}{\partial y} \bigg|_{y=0} \tag{2.13}$$

The walls were also considered to be hydraulically smooth as a simplification, since the metal sheets are considered to be in a clean and polished condition. Hence, there was no need to use any roughness parameters to solve the problem.

At the inlet, conditions were established from the previous studies. Ferro [4] implemented four different inlet velocities, previously seen in Table 2.3, with a normal inflow profile. For the outlet, an uniform pressure condition was set at 0, with the reference level pressure being the atmospheric pressure.

The study made was stationary, since it was made for steady-state conditions. As for the solver, it was used a segregated one. This allows to solve separately the turbulence variables (k and ω), the velocity and pressure, and the heat transfer module (which is going to be analysed next). It was set a two-case termination criteria, where the simulation ended by reaching an iteration error below 10^{-8} for each of the stationary solvers or reaching 500 iterations (last resource). The damping factor used for geometries A to C was 0.5 for all except the turbulence variables, which was 0.35. For all geometries D to E, those values were too high for the simulation to converge. Therefore, it was used a value of 0.2 for all solvers.

Heat Transfer Module

Being over a cooking stove means that the flow entering the exhaust may not be at ambient temperature. Although in the beginning of the cooking activity not a lot of heat is dissipated to the air, the heat released in the peak of the energy spending process can be considerable, changing the air temperature moving into the channels and, with that, its properties. The numerical simulation of the exhaust takes this into account. That was accomplished by running the fluid flow simulations in a non-isothermal option, which adds a *Heat Transfer in Fluids* module that is coupled to the turbulent fluid flow simulation.

Similarly to the fluid flow part of the problem, the heat transfer part undergoes some simplifications. The main one is that the flow is seen as an equivalent to a simple heat flow in a pipe. The wall boundaries represent the metal walls that, to simplify the geometry of the problem, have no thickness and are in contact with both the flow inside of the channel and with the ambient air outside the exhaust. This provides two conclusions for the conditions to be applied in the study: the first one is that the external air temperature is considered to be an ambient temperature of 20°C. The second conclusion comes from the heat transfer type. Since the temperatures in this study do not go above 100°C, it means that any kind of radiation can be ignored. By having walls with no thickness in the simulation, it also means that any kind of conduction it could come via the metal sheets can also be neglected and only its very small influence throughout the fluid will be calculated. This means that the only type of heat transfer considered in this numerical study is convection.

Since the flow is moving inside a channel and is pulled by the fan on the top of the exhaust, this heat flux was considered to be occurring through internal forced convection, affecting the channel walls. Therefore, a boundary condition is set. It is described by Equation 2.14, where q_{wall} represents the heat flux through the walls, h the convective heat transfer coefficient, T_{ext} the external temperature and T the internal temperature.

$$q_{wall} = h(T_{ext} - T) \tag{2.14}$$

The convective heat transfer coefficient h calculation depends on the Reynolds number Re_D and the temperature in the element T. Each equation also depends on the hydraulic diameter D_h, fluid thermal conductivity k, Prandtl number Pr, fluid dynamic viscosity μ and the dynamic viscosity at wall temperature μ_s:

$$h = \begin{cases} 3.66\frac{k}{D_h} & \text{if } Re_D \leq 2500 \\ 0.027\frac{k}{D_h}{Re_D}^{0.8}Pr^{0.3}\left(\frac{\mu}{\mu_s}\right)^{0.14} & \text{if } Re_D > 2500 \text{ and } T < T_{ext} \\ 0.027\frac{k}{D_h}{Re_D}^{0.8}Pr^{0.4}\left(\frac{\mu}{\mu_s}\right)^{0.14} & \text{if } Re_D > 2500 \text{ and } T \geq T_{ext} \end{cases} \tag{2.15}$$

The heated air flow coming via the inlet is the other heat source for the system. This is represented in the simulation as a heat inflow, and it is calculated by Equation 2.16, where U is the flow-stream velocity and ΔH is the enthalpy difference between the point being analysed and the inlet, with α_p being the coefficient of thermal expansion and C_p the specific heat capacity of the fluid.

$$q_{in} = \rho U \Delta H \tag{2.16}$$

$$\Delta H = \int_{T_{in}}^{T} C_p dT + \int_{p_{in}}^{p_A} \frac{1}{\rho}(1 - \alpha_p T) dp \tag{2.17}$$

For all geometries D and E there is an extra condition being imposed. Since the reversed L shaped empty zone left to the entry represents a tiny, 1 mm thick metal L, there should exist some amount of conduction from the heated flow to the metal sheet. However, since it is only in contact with the flowing air inside the channel and its volume is considerably small, it was decided that the extra complexity that the process would bring would not be worth the computational time. So, it was considered that there was no heat flux from that zone ($q = 0$), represented in the simulations as a *Thermal Insulation* condition in the walls around that zone.

COMSOL also takes into account the work done by pressure changes, Q_p and the viscous dissipation in the fluid, Q_v:

$$Q_p = \alpha_p T \bar{U} \nabla p \tag{2.18}$$

$$Q_v = \Big(\mu_T \Big(\nabla \bar{U} + (\nabla \bar{U})^{\mathrm{T}} - \frac{2}{3} \nabla \cdot \bar{U}\Big)\Big) \nabla \bar{U} \tag{2.19}$$

Balancing all the work and heat fluxes entering and leaving the system, *COMSOL* calculates the total heat transfer in the domain with the heat equation (Equation 2.20), the version of the Energy equation presented before (Equation 2.4c) used to perform the numerical calculations, where k is the thermal conductivity.

$$\rho C_p \frac{\partial T}{\partial t} + \rho C_p U \nabla T = \nabla(k \nabla T) + Q_p + Qv + Q \tag{2.20}$$

In this equation, the term $\rho C_p \frac{\partial T}{\partial t}$ is excluded from it since the simulation is performed in steady-state, meaning every term with $\frac{\partial}{\partial t}$ is equal to zero.

The temperature calculations, due to this study being non-isothermal and including turbulence, which becomes a source of energy as well as being an instantaneous random variable. Therefore, the temperature calculation ends up being very complex and using the Reynolds average, just like in the other equations in this study, the temperature is given by this equation:

$$\bar{\rho} C_p \bar{U} \nabla \widetilde{T} + \nabla(-k + k_T \nabla \widetilde{T} = -\frac{1}{\bar{\rho}} \Big(\frac{\partial \bar{\rho}}{\partial \widetilde{T}}\Big)_p \widetilde{T} \Big(\frac{\partial \bar{p}}{\partial t} + \bar{U} \nabla \bar{p}\Big) + \Big(\mu_T \Big(\nabla \bar{U} + (\nabla \bar{U})^{\mathrm{T}} - \frac{2}{3} \nabla \cdot \bar{U}\Big)\Big) \nabla \bar{U} \tag{2.21}$$

where $\widetilde{T}$ is the Favre average of the temperature and it is given by:

$$\widetilde{T} = \frac{\overline{\rho T}}{\bar{\rho}} \tag{2.22}$$

For the Heat Transport turbulence model, the Kays-Crawford model was used. Although this is a simple model compared to the extended version or newer models, it has proven to be a safe and consistent model for near-wall turbulent flow [31]. This model provides an equation in order to calculate the turbulent Prandtl number, Pr_T, presented below, where the turbulent Prandtl number at infinity $Pr_{T\infty}$ takes the value of 0,85 and k is the thermal conductivity.

$$Pr_T = \left(\frac{1}{2Pr_{T\infty}} + \frac{0.3C_p\mu_T}{k\sqrt{Pr_{T\infty}}} \Big(\frac{0.3C_p\mu_T}{k}\Big)^2 \Big(1 - exp\Big(- \frac{k}{0.3C_p\mu_T\sqrt{Pr_{T\infty}}}\Big)\Big) \right)^{-1} \tag{2.23}$$

Mesh

The models of this fluid flow simulation are of a discrete nature, solving the partial differential equations (PDEs) composing the problem through the Finite Element technique, since it is a 2D study. This method creates a mesh by dividing the domain in several smaller parts: elements. To the set of elements filling the entire domain it is called the grid, forming the exact geometry required from the user in the first place.

The size of the elements is essential to the accuracy of the simulation: a more refined grid (with more elements, smaller sized) increases the resemblance to the real case and therefore, increases (in general) the accuracy of the simulation as well. However, that increases as well the computational time, since it requires more calculations to be made. The type of grid also may define the quality of the mesh: it can be a structured, unstructured or hybrid grid. Hybrid grids are a mix of both in the same domain. Structured grids have all the nodes in contact with the same number of elements [29]. It tends to bring better results since they are formed in the most efficient way possible and reduces the computational load of the study. Unstructured grids are the most used, specially in cases with irregular geometry, since in those cases it becomes difficult or even impossible to organize efficiently the elements.

This work goes through different geometries but all meshes are based in the mesh from geometry A. Since that geometry, just like geometries D and E, are made exclusively from rectangular areas, a structured grid with quadrilateral mesh, made by squares and rectangles, was possible to be achieved. For the remaining geometries, since at least part of the geometry is trapezoidal, the *Mapped Mesh* function is applied to those areas when necessary. This is a mesh creating option that still forms a structured mesh with quadrilateral elements, just like the one describe before, which is adaptable to areas close to rectangles formed by non-right angles. This allows for a great quality mesh even with slightly more complex geometries, not affecting the accuracy of the results by changing geometries.

The refinement procedure is controled by the grid refinement ratio h_i/h_1, where h_i is the size of the current element and h_1 is the size of the starting point element. Hence, a smaller grid refinement ratio correlates to smaller elements and a more refined grid. The starting point was $h_i = 0.25$ mm, the element size used in the study that preceded this work [5]. The value of h_i was moved, both upwards and downwards to a total of 9 levels, to verify how fine the mesh should be so it would not affect the final results of the study.

Due to the presence of walls near-flow in the case of this work, and therefore, the presence of a boundary layer were the flow is in contact with the wall, the mesh must be extra refined in that zone.

The compatibility of the chosen model, *k*-ω, with the flows in the near-wall region was essential for its choice, so the no-slip condition can be applied in the walls. Therefore, a wall treatment is necessary to solve the flow near walls. Since wall functions do not provide good results with separated flows due to a lack of correlation to the predicted velocity profiles [32] and the Reynolds number is quite low for a turbulent flow, a *Low Reynolds* treatment was applied. By not using wall functions one must be careful with the value for y^+, the non-dimensional wall distance, defined in Equation 2.24, with u_τ being the friction velocity, defined in Equation 2.25. In order to perform correctly all of the calculations near-wall, in the linear sub-layer, there should be several elements in $y^+ < 5$, with $y^+ < 1$ being the valued normally required in most simulation cases without wall functions.

$$y^+ = \frac{y u_\tau}{\nu} \tag{2.24}$$

$$u_\tau = \sqrt{\frac{\tau_w}{\rho}} \tag{2.25}$$

The boundary layer refinement was made through the *Boundary Layers COMSOL* option, with a stretching factor of 1.2 (in order to keep the smoothness of the mesh) and keeping the number of boundary layers constant at the value of 12 to avoid a numerical error that would occur with bigger numbers, in which the element height would start to decrease before increasing again until the normal height for the remaining mesh, seen in Figure 2.8.

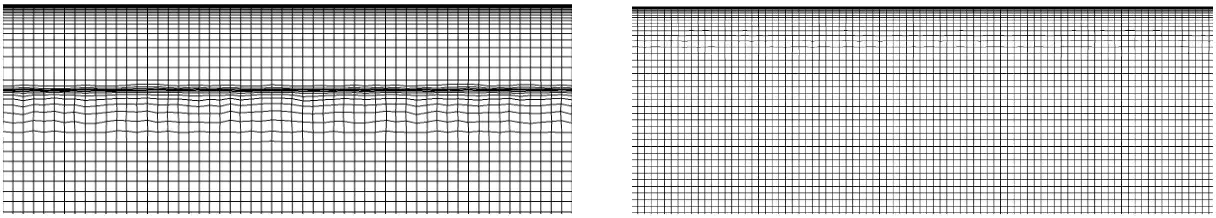

Figure 2.8: Mesh with an error due to excess of boundary layers (left) and a well modelled mesh (right).

Particle tracing simulations

As it was said before, the flow entering the exhaust channels is not a simple air circulation. Instead, due to the cooking activities performed underneath it, it is a two-phase flow, which contains a set of particles in a continuous phase: the air fluid flow. That set is mainly composed by grease particles, which can end up depositing inside the channels of the exhaust, causing not only an obstruction to the fluid flow but also a decrease in the filtering efficiency and even some dripping to the stove or other objects beneath the exhaust. Therefore, the particle movement had to be studied as well. For that, it was used the *Particle Tracing* module in *COMSOL MULTIPHYSICS®*. This module can be used in this case, since the volume fraction of the solid phase (particles) should be inferior to 1% due to the small size of the particles being studied. It is then considered to be either a sparse, dispersed or dilute flow. For cases where the solid phase surpasses that percentage, the flow is named as dense, thus the particle tracing module can not be used. In the case of this work, due to the very small diameters of the particles, it is considered to be a sparse flow, where a one-way coupling is applied. This means that the particle phase movement is influenced by the continuous fluid flow phase, but the particles do not affect the fluid flow phase since the flow is not dense enough. It also means that the particles are not big enough to affect each others movement. Therefore, the particle tracing module could be used after the fluid flow simulations were completed, in order to apply a time dependent simulation to the movement of the particles inside the fully developed, steady-state fluid flow motion. If the particles were slightly bigger, it would be a case of a two-way coupling, or dilute flow. Would this case be needed to be studied numerically, both simulations would have to be run together as there would be a two-way interaction between the particles and the fluid flow: the flow affects the particle movement and, in its turn, the particle movement would affect the flow that is immersed in. That would also happen in a four-way coupling (or dilute flow) case, with the difference that the particles would be big enough to also influence each others movement. These additional interactions would also increase the computational time of the simulations, since each collision and movement would have to be described and calculated in further detail, costing more time to process. Figure 2.9 shows a summarized scheme with the several particle models.

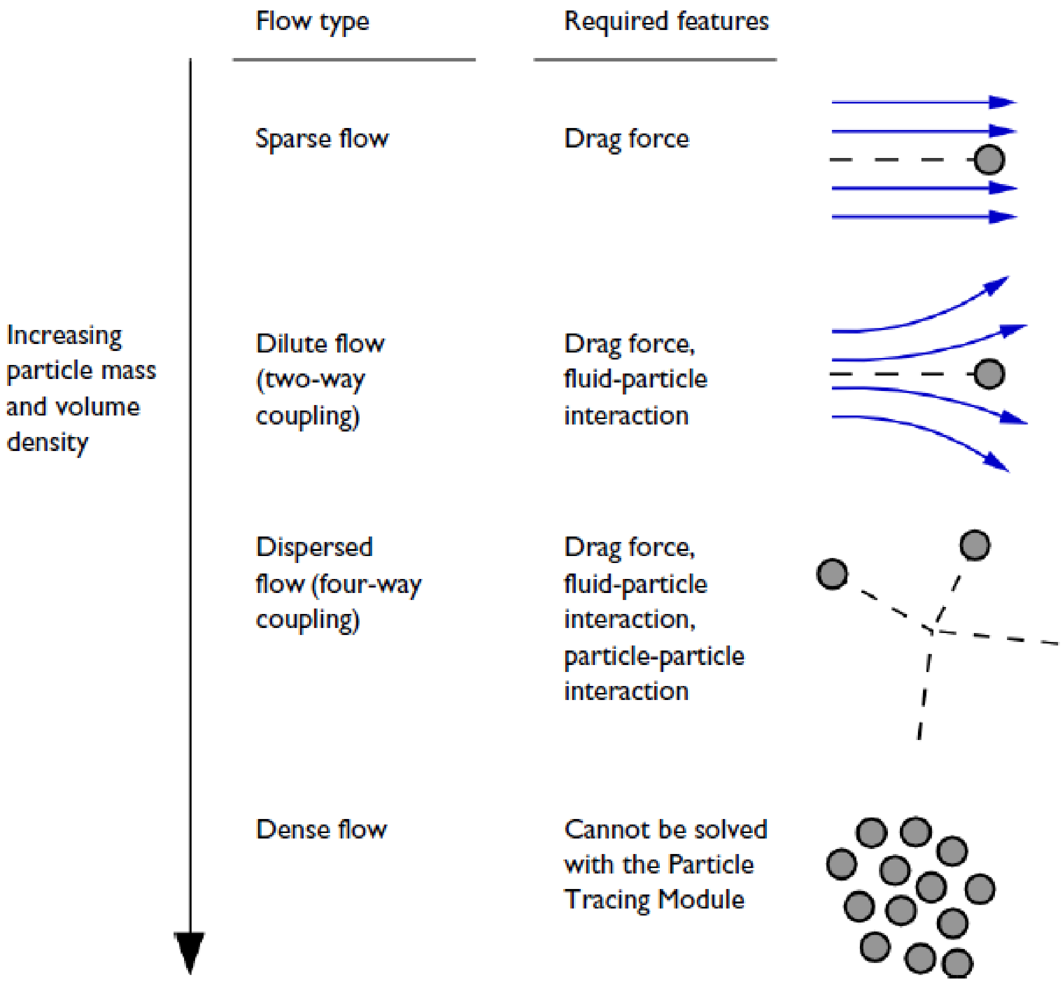

Figure 2.9: Schematic with the types of particle modelling (extracted from [33]).

Just like it is referred to in the image, for the case of this study, drag is the main force acting in the particles and influencing its movement. Since the particle's relative Reynolds number (Equation 2.26, where u is the fluid velocity, v the particle velocity and D_p the particle diameter) in this work is in the range of 1 to 800 [5, 33], the drag force (Equation 2.27, where m_p is the mass of the particle) is calculated by the Schiller-Naumann law, which includes the influence of the particle response time, τ_p (Equation 2.29, where ρ_p is the particle density). This means that the drag force is inversely proportional to the Stokes number mentioned before in Equation 1.4, that is, if a bigger drag force influences the motion of the particle, then its Stokes number should be smaller.

$$Re_p = \frac{\rho(u-v)D_{\mathrm{p}}}{\mu} \tag{2.26}$$

$$F_D = \left(\frac{1}{\tau_p}\right) m_p(u-v) \tag{2.27}$$

$$\tau_p = \frac{4\rho_p D_p^2}{3\mu C_D Re_p} \tag{2.28}$$

with $\mathrm{C_D}$ being the drag coefficient, defined as:

$$C_D = \frac{24}{Re_p}(1 + 0.15{Re_p}^{0.687}) \tag{2.29}$$

However, drag is not the only required force in the case of this work. Being a flow with considerate mass, the gravity force (F_g) must be also taken into account. Therefore, the gravity force is also present in the study, through Equation 2.30, where g is the gravity vector and takes the value of 9.80685 $\mathrm{m/s^2}$.

$$F_g = m_p g \frac{\rho_p - \rho}{\rho_p} \tag{2.30}$$

With the study including near-walls to the flow, some studies were run to test the effect of shear induced lift forces on the particle movement and deposition. Since it is near wall, the *Wall induced* lift force is selected, a corrected version of the Saffman model to flows in channels. Therefore, the lift force F_L will be calculated via Equation 2.31, where r_p is the particle radius, L is the distance between walls, u_{par} is the velocity of the fluid parallel to the nearest wall and G_1 and G_2 are functions to the non-dimensional particle distance to the wall s.

$$F_L = \rho \frac{r_p^4}{L^2} \beta(\beta G_1(s) + \gamma G_2(s)) \tag{2.31}$$

where $\beta = \mid \mathrm{L} \, \nabla \, u_{par} \mid$ and $\gamma = \left| \, \frac{L^2}{2} \, (\nabla \, u_{par}) \, \right|$. According to [34], this force should be taken into account even for one-way coupled cases. However, this is mostly for laminar flow cases since the eddies in the turbulence flow can overlap these inertial forces and redistribute evenly the particle location [35]. Therefore, for the final results, the lift force was not applied in the studies.

Since the flow in this study was turbulent, the effects it might provoke on the particles should also be analysed. Those effects are represented by the turbophoretic force, F_{Tb}, which can be modelled in the particle tracing module via the *turbulent dispersion* option. This will simulate the effect of the turbulent eddies from the flow on the particle movement. In order to include the anisotropy of the turbulence also in the boundary layers, the sub-option *Continuous Random Walk model* was selected. This model chooses the velocity and position of each element of fluid in a stochastic manner, via a Markov process. This is, although it is a random process, the following values are influenced by those in the present moment. The time interval which can affect the values being calculated is given by the Lagrangian time scale, τ_L, previously seen in the Stokes number in Chapter 1.2.3, calculated in this model like it is presented in Equation 2.32.

$$\tau_L = C_L \frac{k}{\epsilon} \tag{2.32}$$

with k being the turbulent kinetic energy, ϵ the turbulent dissipation rate and the dimensionless coefficient C_L being the Lagrangian time scale coefficient. Depending on the study, C_L can take a value from 0.14 [36] up to 0.96 [28, 33], which was the value used in this work. The fluid velocity (u) is then solved in time by calculating the following Langevin equation in the x and y directions:

$$d\left(\frac{u}{u_f}\right) = -\frac{u}{u_f}\frac{1}{\tau_L}dt + \zeta\sqrt{\frac{2dt}{\tau_L}} + \frac{1}{3u_f}\frac{dk}{dx_i}\frac{1}{1+St}dt \tag{2.33}$$

where the instant velocity fluctuation u_f is given by $u_f = \sqrt{\frac{2}{3}k}$.

The heat flux coming from the stove and cooking tasks can also affect the particle motion via the thermophoretic force, F_{Th}, as it was explained in further detail previously, in Chapter 1.2.3. The Talbot model, seen as accurate for all types of flows and Knudsen numbers [37], was the one chosen. Therefore, the thermophoretic force was calculated for the numerical simulations according to the Equation 2.34, where Kn is the Knudsen number, T is the fluid temperature, C_s, C_t and C_m are thermophoretic correction factors that take the values of 1.17, 2.2 and 1.146, respectively [33]; and Λ is the ratio between the fluid thermal conductivity, k, and the particle thermal conductivity, k_p $\left(\Lambda = \frac{k}{k_p}\right)$.

$$F_{Th} = -\frac{6\pi D_p \mu^2}{\rho}\frac{C_s(\Lambda + C_t Kn)}{(1+3C_m Kn)(1-2\Lambda+2C_t Kn)}\frac{\nabla T}{T} \tag{2.34}$$

For this equation it is also given the air molar mass (M_{air} = 28 g/mol) and the particle thermal conductivity is taken from [38], k_p = 0.165 W/m.K. The option to *use piecewise polynomial recovery on field* is also activated, in order to smooth the temperature in the fluid and provide a more accurate solution to the simulation.

The existence of Brownian forces was also acknowledged. However, particles with a diameter over 0.5 μm are not affected by these motions [22], hence not being considered in this study right from the start.

Joining all the forces F affecting the particle, its movement and momentum will be determined by a first order Newtonian formulation, composed by the Newton's second law (Equation 2.35):

$$\frac{d}{dt}(m_p v) = F = F_D + F_g + F_L + F_{Tb} + F_{Th} \tag{2.35}$$

where v, the particle velocity is equal to the time derivative of the particle position, q:

$$\frac{dq}{dt} = v \tag{2.36}$$

For the particles being studied, it was attempted to capture all the types involved in a normal act of cooking, more focused to the typical Portuguese cuisine (using olive oil) or fast foods (cooking hamburguers and others). The study by Kuehn et al. [10] was the one focused on to obtain a typical particle diameter and density. Together with the studies performed by Monteiro [5] about buoyancy forces from the stove to the exhaust inlet and knowing that the particles are modelled as spheres in *COMSOL*, the particle diameters (D_p) to be studied were defined as in the range between 10 and 100 μm, while the particle density (ρ_p) was kept equal to the one used by Monteiro[5], 980 kg/m^3. The values for the particle dynamic viscosity (μ_p) and surface tension (σ_p) were also kept the same as in the previous study [5]: $\mu_p = 52$ mPa.s and $\sigma_p = 0.0335$ N/m. The particle diameter was changed for each study of the same inlet velocity and temperature in order to check how it affects the deposition in the walls, while the temperature of the particle was assumed to be constant and equal to the fluid temperature, as its variation would not affect the results in a large scale and would bring a bigger computational effort, resulting in a larger computational time.

So, for the inlet it was established an uniform distribution for the particles along the 10 mm wide entry, with a batch of 100 particles being released each 0.04 seconds during a 1 second time span. For the outlet, seen as an equivalent to the filter in the real exhaust for this study, it was decided to apply a freeze condition. This option stops the particle when in contact with the geometry boundary but keeps the particle velocity registered, while the stick option would automatically bring the particle velocity to zero. This could prove useful when trying to analyse if a particle arrived from a zone with a higher or lower velocity (from recirculation zones, for example). For the walls, the option to select the condition of bouncing was available. However, for the small size and the viscosity value of the particles in study, plus the randomness created from the turbulent flow, that option was not worth the extra computational effort and time that it also brought to the simulation. So, the condition selected for the walls was freeze as well. However, due to their small volume, the particles stuck in the wall did not add any extra height to the walls, a reasonable simplification that also saves time to the simulation process. This way, the condition imposed allowed to see the progress of the continuous depositing of the particles along them.

For that same reason, the study was made time dependent. In order to maximize the accuracy of the study, the time step defined had to be quite small. However, it could not be so small that it would cause the simulations to be too computationally heavy. So, it was defined a time step of 0.005 seconds, with a total duration of 1.5 seconds, based on previous works [5]. This gave 0.5 seconds after the last batch of particles was released from the inlet in order try and stabilize the results, without adding too much calculations to the study. Although this interval is quite small compared to the time length of a normal cooking activity, which can take several minutes or even hours, it is a time step that, during a regular cooking process, can be taken as a steady-state. This means that the particle production should continue like the one studied in this work during the next several seconds or minutes of cooking. Therefore, the particle deposition can be analysed as a percentage for each section of the exhaust and generalized to the entirety of the cooking process.

The particle tracing study was applied to all of the geometries presented before in the Chapter 2.2.1 (except for the optimized E geometries) in order to perform a more complete analysis for each of them, since a gain in the pressure loss section of the study does not guarantee that the results for the particle tracing study should also be positive. Therefore, it might be necessary to do a compromise between both subjects of this work. Each geometry was analysed for a set of 10, 15, 20, 25, 50 and 100 μm, with each diameter being studied separately. For each different inlet velocity and temperature it was also done a separate study. It was decided to analyse only the most extreme cases for the velocity: $V_{min} = 2.02$ m/s and $V_{max} = 2.37$ m/s. For the temperature, 3 cases were studied: the ambient temperature, $T = 20°$C, was the basis for a functioning case where the exhaust is just extracting air. It allows also a comparison to future experimental cases. For a worst case scenario it was taken from Bhatia [39] a high temperature from a more commercial case: $T = 60°$C. Nonetheless, it was also taken a temperature value from a regular kitchen cooking case. That value was taken by a thermocouple, validated in a way further explained later in Chapter 2.3, and it gave a value of $T = 38°$C. To simplify the study, the third, real case was studied at a temperature of $T = 40°$C.

The mesh is the same used in the fluid flow study. For the solver, it was used a fully-coupled direct solver, with a relative tolerance of 10^{-5}.

2.3 Experimental Setup Overview

To evaluate some of the values obtained in the numerical part, this work adds an experimental part as a complement. By simulating the flow in a real case, with a similar geometry, and measuring the pressure losses throughout the channel, it is guaranteed that the results obtained can be translated into reality. Since the objective is to analyse the results and compare with the numerical part, the experimental setup is built around the numerical geometry and not the real exhaust (since that would also add an enormous level of complexity to the work, similarly to a 3D numerical simulation). This is done via an acrylic prototype, initially used by Ferro [4], which was slightly improved for this work.

The setup is composed by acrylic plates glued to each other, in order to form a 3D version of the 2D geometries studied numerically, with a width of 300 mm. Although it is a 3D geometry, all of the data was collected in a single 2D cross-section, in the middle of the setup (in terms of width), being that the width for this setup is maximized in order to avoid any 3D effects in the results. Since the objective was to simulate a different geometry, it was 3D printed in Poly-Lactic Acid (PLA) a chamfered entry with a 10 mm deviation to the inside in the 90 degree corner zone in order to simulate geometry B, as it can be seen in Figure 2.10. This part was glued to the inside of the acrylic entry, which obliged the outside wall to be moved.

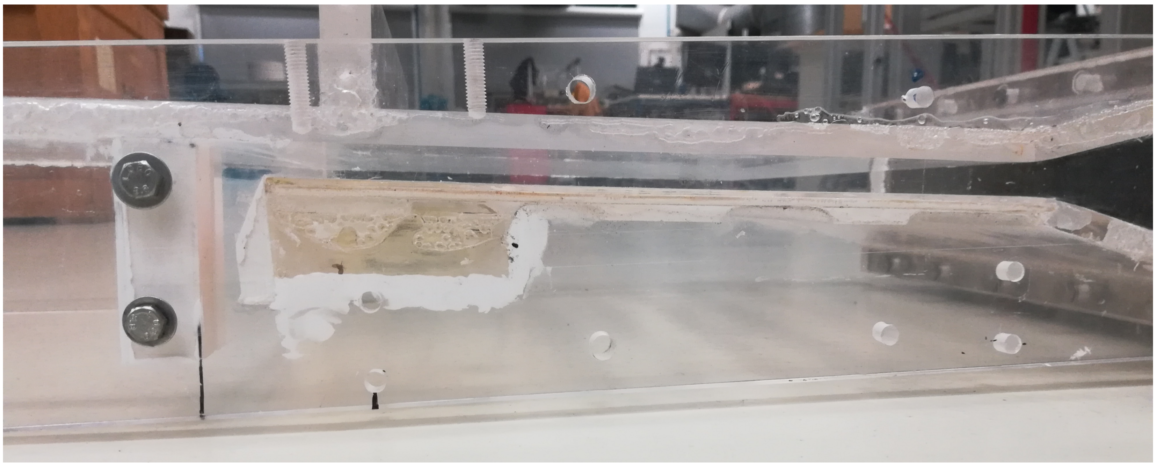

Figure 2.10: Real geometry tested with the experimental setup.

This allowed the outside wall to be designed in a way that could be moved if new, different parts had to be tested in the future. Therefore, two new, symmetric parts were 3D printed, also in PLA, with two holes allowing to be threaded and fastened by 2 M6 bolts each, one to each side of the acrylic setup. This part, with a length of 20 mm, a width of 32 mm and a height of 63 mm, has a 16 mm long, 3.15 mm deep cut along all of the height in one of the sides. This allowed a quartz glass with the same thickness (3,15 mm) and height (63 mm) to be glued to it, creating all 3 parts a new outside wall that replaced the previous acrylic wall which was glued to the setup (Figure 2.11), with the advantage of being movable and the quartz glass allowing a clean passage to any laser beams. This will provide better conditions for any future Particle Image Velocimetry (PIV) tests to be made in future studies with this setup. The geometry had the same channel thickness from the numerical studies (10 mm), with the only difference being the entry zone, being slightly bigger due to the constraint in the height of the quartz glass.

Figure 2.11: Image of the new outside entry wall for the experimental setup, with 3D printed parts and quartz glass.

To the acrylic part, a convergent metal duct was bolted by 11 M6 screws that, in turn, was connected to an electric fan by a hose. The electric fan, which had a nominal voltage of 230 V, was responsible for the air suction, simulating the same effect made by a similar fan in the real perimetric exhaust, allowing the airflow through the acrylic channels. The fan was powered by a VARIAC which provided a voltage between 0 and 240 V, being the voltage applied the one that determines the power output from the fan and, therefore, the inlet mass flows and velocities. The voltage values corresponding to the inlet velocities were taken from [4] and are provided in Table 2.4.

Table 2.4: VARIAC values corresponding to the channel inlet velocities (adapted from [4]).

	VARIAC Voltage [V]	Inlet Velocity [m/s]
P_1	100	2.02
P_2	110	2.08
P_3	120	2.21
P_4	130	2.37

Just like in the numerical study, the only losses assessed in this part of the work are the local pressure losses, evaluated by the same dimensionless parameter K, the local pressure loss coefficient. For that, pressure had to be monitored by a set of pitot tubes (3 in Figure 2.12). These were connected to a *Sensirion SDP1000-L* pressure sensor (2 in Figure 2.12), which was connected to an *Arduino* microcontroller (1 in Figure 2.12).

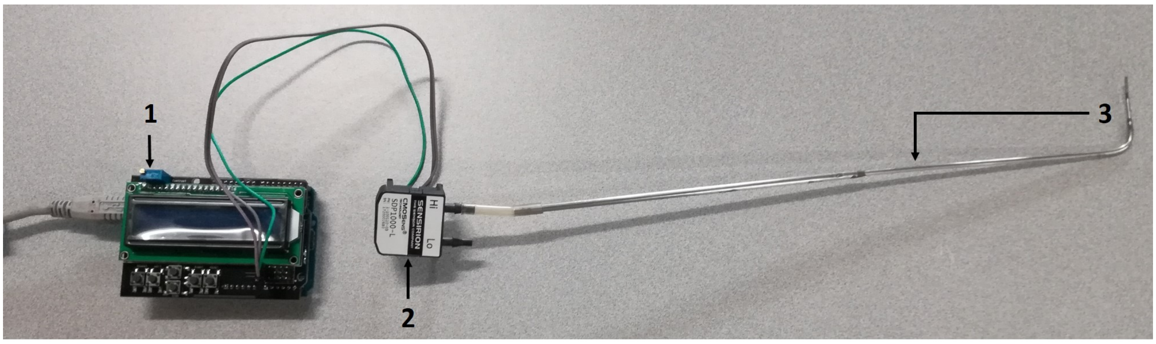

Figure 2.12: Image of the setup used to gather experimental data.

The pressure sensor used is fed by a power supply of 5 V and measures a pressure differential Δp from -20 to 500 Pa, translated into an analog signal output that goes from 0 to 5 V. That output goes directly to the *Arduino*, which is also powered by a supply of 5 V, where it is transformed to a digital signal and processed through a program kindly granted by João Cunha, to whom I am grateful for the help provided.

The setup was prepared by partially disassembling it, since it was in a poorly maintained form. To correct those imperfections one of the side walls was dismounted, as well as the outside entry wall being replaced by the 3D parts and quartz glass wall. During the process, the 3D printed parts facing the flow were sanded up to 250-grit size before being either glued together with the quartz glass and mounted in the setup or glued at the entry zone. The acrylic walls were also polished, all in order to guarantee a smoother and cleaner surface which should improve results not only in the pressure measurements made in this work but also in future PIV tests. Nevertheless, not all of the glue gaps could be corrected, so some losses could still occur. Gaps in the setup were corrected, externally when internally was not possible, with silicone, including a tiny spacing near the 3D parts on the new entry wall. Another very small gap could be seen under the quartz glass but no silicone paste was used there so it would not harm any future PIV measurement. When ready to be tested, the whole setup was put in a supportive structure with extra supports in a table to make sure the hose is kept straight and the fan at the same level compared to the remaining setup. It was made sure that the flow near the entry zone would not be disturbed by the structure and that the channel was at the correct angle, measured by a digital protractor, so it would not influence the results. Figure 2.13 shows the setup in the support structure and an example of how the silicone was used to stop possible air leaks throughout the setup.

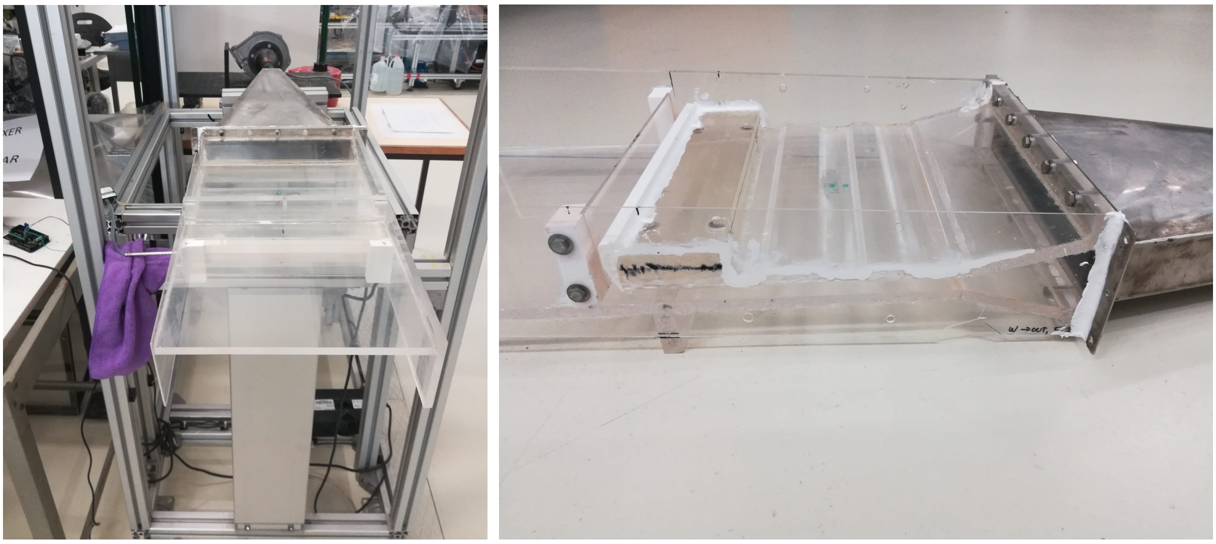

Figure 2.13: Experimental setup mounted in the structure (left) and in detail (right).

The data measured, static pressure, was retrieved in two different ways: first, a single pitot tube measurement was taken, at the same distance from the simulation (60 mm after the corner), where the flow has already returned to a fully developed condition, through a 1mm hole from the top wall of the acrylic setup. This tube was connected to the *High* entry of the pressure sensor while the *Low* entry was left unconnected, that is, at atmospheric pressure. This recreates the same method used in [4] to evaluate the pressure losses in the acrylic setup. The second method only diverges in one point: the *Low* entry, left unconnected in the other method, is now also connected to another pitot tube. It is placed inside and before the entry (below the PLA part) to make a pressure differential between the end and the entry of the channel instead of comparing the pressure after the corner with the atmospheric pressure. This is outlined in Table 2.5, with the first method mentioned from now on by *Single tube method* and the second *Double tube method*.

Table 2.5: Pressure acquisition methods and measurement locations.

Δ p = p_1 - p_2	p_1	p_2
Single tube method	Atmospheric pressure	Channel outlet pressure
Double tube method	Entry level pressure	Channel outlet pressure

The pressure sensor used as a typical measurement error of 0.1%. However, according to Figure 1 of the product's datasheet [40], the error percentage may reach up to 10% for small pressure differentials (under 25 Pa, with the error percentage starting to increase considerably from 50 Pa). Since that is the order of magnitude the results are expected to fall in, their analysis should take this factor into account.

There is also an error associated to the length of the hose that connects the pitot tube to the sensor entry, with a loss of 0.8% per meter of hose. The tube connecting the channel measurements has a hose with less than 5 cm, a very small length. For the entry level tube, the connecting hose has a length of approximately 0.2 m, which gives an error of around 0.16%. Since the error is quite under 1% and also taking into account the previously referred to error for low differential pressures, it is considered that both hoses have losses of a negligible order.

The ambient temperature of the room of where the experiments took place does not affect the accuracy of the sensor. It was controlled by a thermocouple, validated before the start of all experiments by a correct temperature measurement inside a small room with controlled environment (controlled ambient temperature). Although the real exhaust does have a inlet flow temperature higher than the one tested here, it was impractical to do it with a similar temperature. So, the results of the experimental part should be compared to the simulations with a similar temperature, 20°C, and in this way it is also possible to compare the results with the ones obtained in [4]. The experiment was made 10 times for each method, 5 for the maximum inlet velocity and 5 for the minimum inlet velocity. For each experiment, data was collected during a time interval of 15 seconds, some seconds after the fan started, in order to stabilize the flow and avoid any perturbation that could influence the inputs. After gathering all of the data for each individual experiment, the values were processed and filtered in an Excel file.

Chapter 3

Results

In this chapter, the results from both numerical and experimental parts of this work are presented. Firstly, the numerical results are described and analysed, starting with the initial geometry, followed by all the alternatives made. In each of them, the fluid flow is analysed first, with the effect of the temperature and inlet velocity on pressure losses and flow characteristics being investigated. This is followed by the particle studies, showing their deposition variation across the different temperatures and velocities as well. The experimental part is then presented, with the analysis focused in the pressure losses, with a comparison to the numerical case but also in the data collecting method for the present case.

3.1 Initial Geometry

To begin this study, geometry A, the initial geometry, equal to that studied by Monteiro [5], was analysed for all values presented in Table 2.3. This allows not only to see how the flow and its parameters change with the inlet velocity, making it possible to compare with the tendencies verified in [4], but also to investigate how the same parameters change with the flow temperature. This will also serve as a base result to compare with the following geometry improvements.

However, to make sure the results are accurate, a mesh refinement was made. As it was referred to before in Chapter 2.2.2, the starting element side size was $h_i = 0.25$ mm, with studies performed for 9 different values, corresponding to the respective grid refinement ratios h_i/h_1 seen in Table 3.1. A smaller value for the grid refinement ratio corresponds to a domain with more elements, therefore, more refined.

Table 3.1: Values for the mesh refinement and respective grid refinement ratio.

Element side size, h_1 [mm]	1	0.75	0.5	0.38462	0.3125	0.25	0.225	0.2	0.1875
Grid refinement ratio, $\frac{h_i}{h_1}$	4	3	2	1.538	1.25	1	0.9	0.8	0.75

The parameter chosen in order to verify the mesh refinement was the size of the recirculation zone in the bottom wall of the exit zone, designated from now on as the *bottom recirculation length.* As it can be seen in the graph from Figure 3.1, the value for the bottom recirculation zone goes up with the increase in elements, converging to a value, as it is expected.

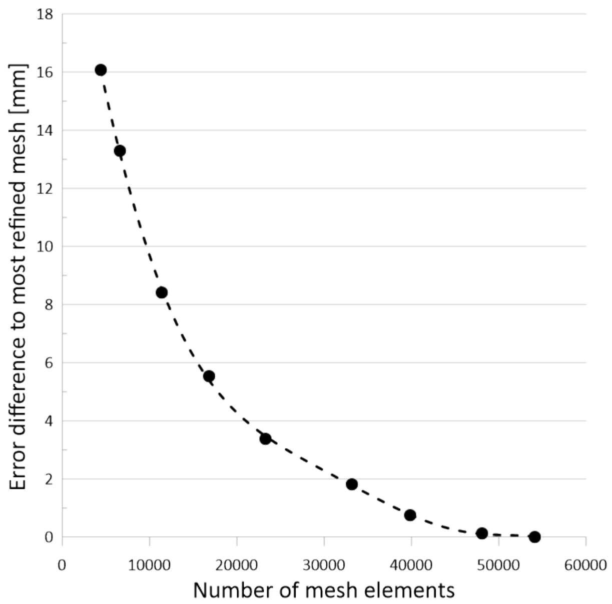

Figure 3.1: Bottom recirculation length evolution with the mesh refinement.

Hence, the following studies were all performed for the finer mesh, with an element side size of 0,1875 mm.

3.1.1 Pressure losses in the channel

One of the ways to reach the objective of this work is by analysing the pressures losses and flow parameters inside the geometry being studied. This can be done, as it was explained before, by checking the local pressure loss coefficient K for each case, inspecting as well what happens to the main causes for that pressure loss: the recirculation zones. This kind of geometries, with sharp corner angles, end up causing flow separation in two different recirculation zones: the *bottom recirculation zone*, seen in Figure 3.2 in orange, with its length already mentioned as the bottom recirculation length from the interior corner to point a; and the *top corner recirculation zone*, represented in blue in the figure below, with the length from the top corner to point b designed as the *top recirculation length* and the the vertical dimension from point c to the top corner named as *vertical recirculation length.*

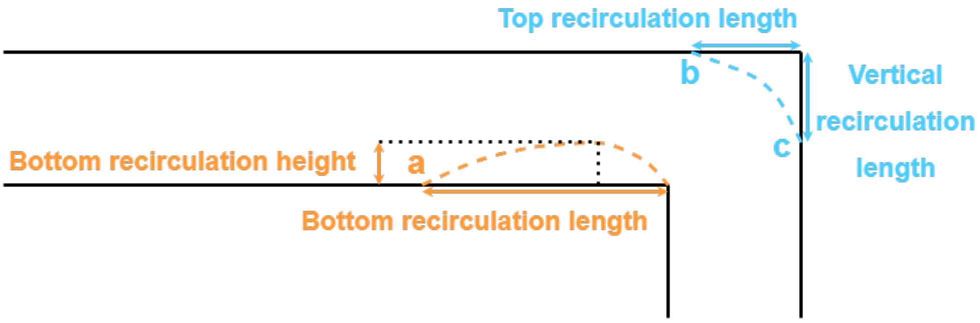

Figure 3.2: Basic layout for recirculation zones in geometry A (adapted from [4]).

The points in the previous image represent separation (c) and reattachment (a, b) positions of the flow. The separation is caused by the 90 degree corner of the geometry, inducing an adverse pressure gradient $\left(\frac{dp}{dx}>0\right)$ that causes the velocity in the near-wall zone after the corner to reverse [8]. The flow reattaches further ahead, with the help of turbulent diffusion, represented in the numerical studies by an increase of the turbulent viscosity, μ_t. Those points are the exact locations where the flow is reversing its direction, that means that the flow velocity derivative at the wall will be zero $\left(\frac{\partial U}{\partial y}=0\right)$ and, therefore, the shear stress at the wall in that point will also be zero.

In the top corner recirculation zone, the results show a clear tendency. Points b and c get closer to the corner when the inlet temperature increases and the velocity decreases. That can be seen in the graphs from Figure 3.3, with both top and vertical recirculation lengths decreasing in those situations. That was expected, since a higher temperature correspond to a lower ρ and higher μ, which will retard the separation point. A lower velocity also allows the flow to better adapt to the geometry, reducing the size of the recirculation bubble. The results translate to a slightly bigger area for this recirculation zone with higher velocities, which is an equal outcome as it was obtained by Ferro [4].

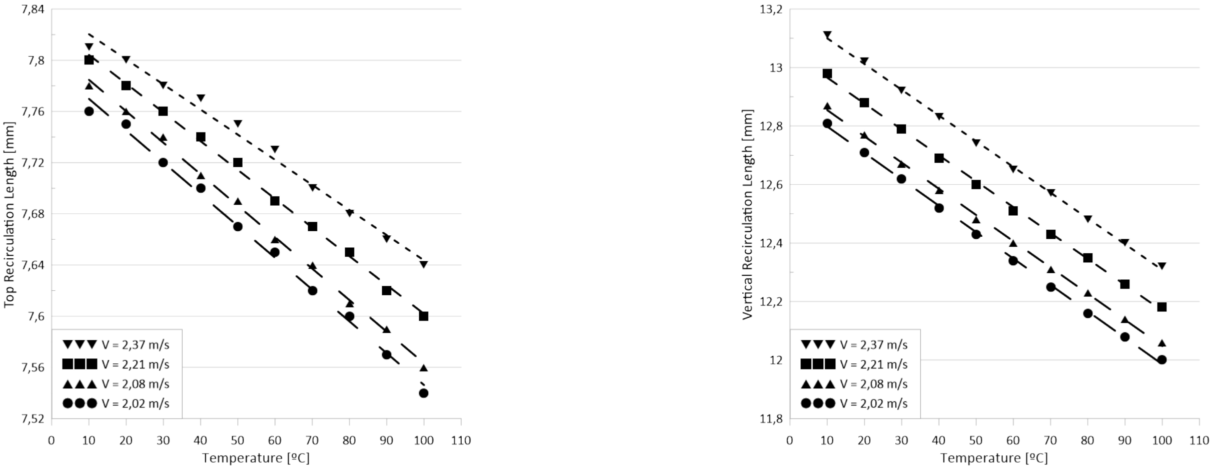

(a) Top recirculation length.

(b) Vertical recirculation length.

Figure 3.3: Variation of top (a) and vertical (b) recirculation length with inlet temperature and velocity.

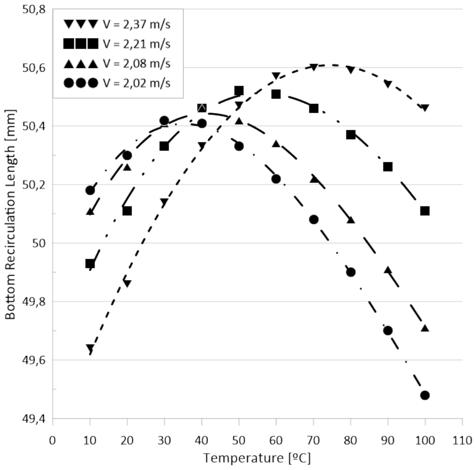

Figure 3.4: Variation of bottom recirculation length with inlet temperature and velocity.

For the bottom recirculation zone, the results make the analysis more complex since it shows that the bottom recirculation length has a peak value for a certain inlet temperature instead of a linear dependency on velocity. Peak values for this length still increase with velocity but also increase with temperature, as seen above in Figure 3.4. This peak in the bottom recirculation length seems to happen around the same interval in terms of Reynolds number: from 2350 to 2550.

The existence of a recirculation zone after the corner can also induce a choking effect to the channel. Since the inside of the recirculation bubble includes a reverse flow, this means that part of the channel height has a total flow rate of zero, reducing the useful height for the air flow and creating a bottleneck. This causes flow acceleration in that useful zone of the channel which brings losses to the flow. The *bottom recirculation height* of the bubble was, then, also analysed. However, because the method to obtain such results from *COMSOL* was highly under-optimized, it was opted to check the results just for the same temperatures considered for the particle cases and for the minimum and maximum velocities. The results, presented in Table 3.2, are all obtained in the same vertical section, 12 mm to the left of the 90 degree corner. It is also noticeable that these results barely change with both velocity and temperature changes, following a trend similar to Ferro [4]. The values are also close to the ones obtained in that same study, although being smaller to a small extent.

Table 3.2: Values obtained for bottom recirculation zone height in geometry A.

Temperature [ºC]		20	40	60
Bottom recirculation height [mm] for:	V_{min}	4.53	4.52	4.50
	V_{max}	4.54	4.53	4.52

All of the previous parameters characterize the flow but the main parameter to be examined is K (Figure 3.5), which allows the pressure losses to be analysed and compare the energy performance between all geometries.

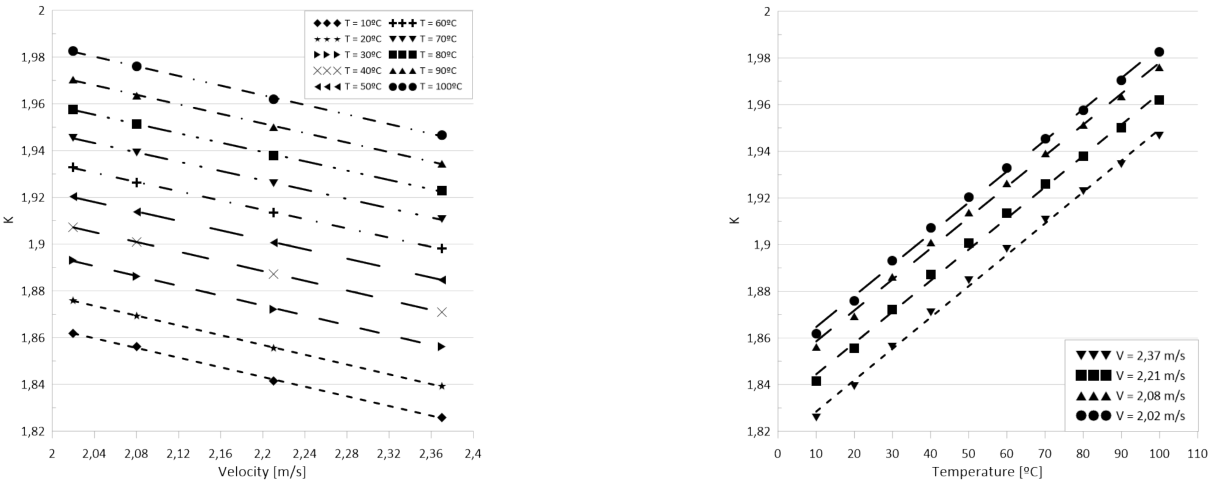

(a) Variation of K with velocity.

(b) Variation of K with temperature.

Figure 3.5: Values of K for geometry A and their dependence on temperature and velocity.

Figure 3.5(a) presents the relation of K with the inlet velocity to all inlet temperatures. The values vary linearly with little error and show a similar tendency to the one obtained by Ferro [4] in his experimental study to the channel. It is similar to the results of Monteiro [5] as well, both in terms of tendency and order of magnitude. It is also coherent with the very definition of K, since it includes the squared velocity in the fully developed section of the channel, which depends on the inlet velocity, in the denominator of the definition. This counteracts the lower losses in pressure that comes from a lower inlet velocity. Therefore, although it spends more energy, the most efficient use of the exhaust comes at maximum power.

The variation of K with the inlet temperature, shown in Figure 3.5(b), is also nearly linear for the four inlet velocities. It also shows a bigger influence of temperature in the values of K since there is a slightly higher slope in this graph. Although there is, once again, a decrease in the pressure drop for higher temperatures, the lower density values cause an increase in the local pressure loss coefficient and thus, a decay in the energetic efficiency of the exhaust. The losses in energy to the colder walls also help to explain this tendency of K with temperature. The heat transfer can be seen in Figure 3.6(a), where the temperature variations throughout the channel are represented. Comparing to Figure 3.6(b), where is shown the velocity field for the same study, it is observed that in the recirculation zones, where the value for heat transfer coefficient peaks, the temperatures reach lower values easily. However, for the remaining zones, the temperature only decreases in a more significant way near the boundary layer zones, with the flow in the center of the channel, the zone further way from the cold walls, barely decreasing more than 5°C.

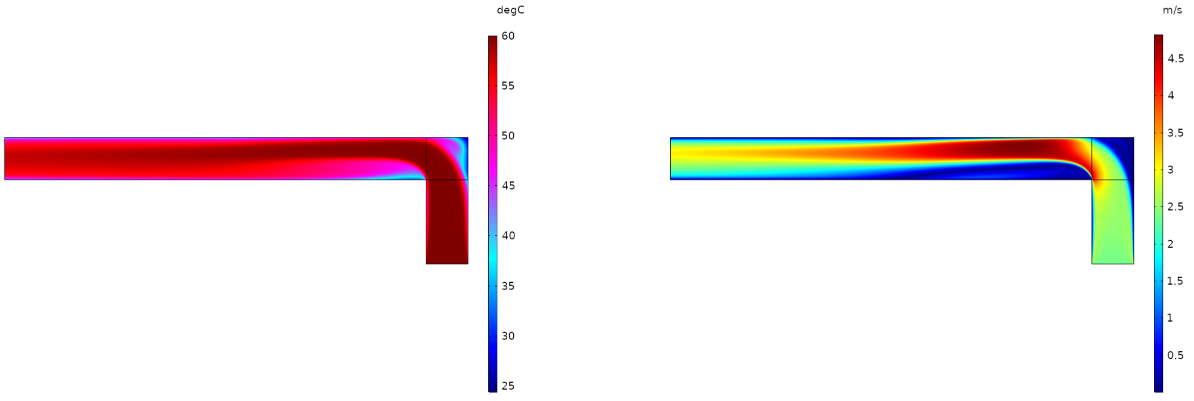

(a) Temperature results

(b) Velocity results

Figure 3.6: Results of the simulation on geometry A for V_{max} and inlet temperature of 60°C.

3.1.2 Particle tracing

In the studies for particle deposition, tests were made to determine which forces affecting the particle movement were to be simulated. Before those were performed, the lift forces were disregarded right at the start since according to Lashgari et al. [35], the turbulent eddies in the flow overlap any effect the lift forces could have in the particles. The turbophoretic force would represent those turbulent effects to the particles, through the *turbulent dispersion* option in *COMSOL*. However, the results remained nearly unchanged with the incorporation of this force in these studies, while it increased the time necessary to run the study by over 20 times. Hence, it was decided not to include turbophoretic forces in the particle tracing studies. The same decision was made for the thermophoretic forces since the effects are valid only for particles in a range of diameters smaller than what is presented in this work [19]. Thus, the forces acting on the particles in the following studies are the drag force, F_D, and the gravity force, F_g.

As previously mentioned, the studies were carried out for the maximum and minimum inlet velocities, with three inlet temperatures corresponding to the ambient temperature, T = 20°C, measured temperature in a home kitchen, T = 40°C, and an extreme case corresponding to commercial kitchens, T = 60°C. These six variations were studied for six different particles diameters, each in a separate study. The results are presented always in percentage, since the studies are all made with the same total quantity of particles, released at the same time as explained previously in Chapter 2.2.2.

Since the particles can collide in different zones of the channel, it was decided to name the different walls for a better interpretation of the problem. Those are presented below, in Figure 3.7.

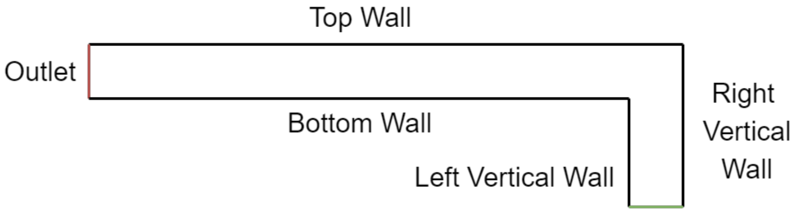

Figure 3.7: Wall nomenclature used in geometry A for the particle tracing study analysis.

Firstly, the influence of the particle diameters is going to be seen. Table 3.3 presents the results of the particle tracing simulations for all diameters at maximum velocity, V = 2.37 m/s, and ambient temperature, T = 20°C.

Table 3.3: Deposition percentages for each diameter in geometry A with V_{max} and T = 20°C.

D_p	Top Wall	Outlet	Top Corner Recirculation	Left Vertical Wall	Right Vertical Wall
10	0	99.88	0.12	0	0
15	0	98.88	1.12	0	0
20	39.65	49	11.35	0	0
25	90.58	9.23	0.19	0	0
50	99.73	0	0	0	0.27
100	100	0	0	0	0

The results have equal tendencies to those obtained by Monteiro [5]: smaller particles are directly almost entirely to the outlet, which represents the filter in this work. This was expected because due to their very small mass, they also have a small Stokes number. Particles with a small Stokes number are, as referred before, expected to follow the streamlines of the flow, decreasing the chance of colliding with a wall or heading towards a recirculation zone. Bigger particles, with more mass and a bigger Stokes number, are more affected by their inertia and deviate from their original streamline easily. Hence, all the particles with D_p = 100 μm hit the top wall and with a larger diameter, more particles get stuck in the same wall, closer to the entry zone. That can be seen in Figure 3.8, where a comparison is made between the top wall deposition of particles with 25 (Figure 3.8(a), particles in green) and 50 μm (Figure 3.8(b), particles in blue), in the case of maximum inlet velocity and inlet temperature of 20°C.

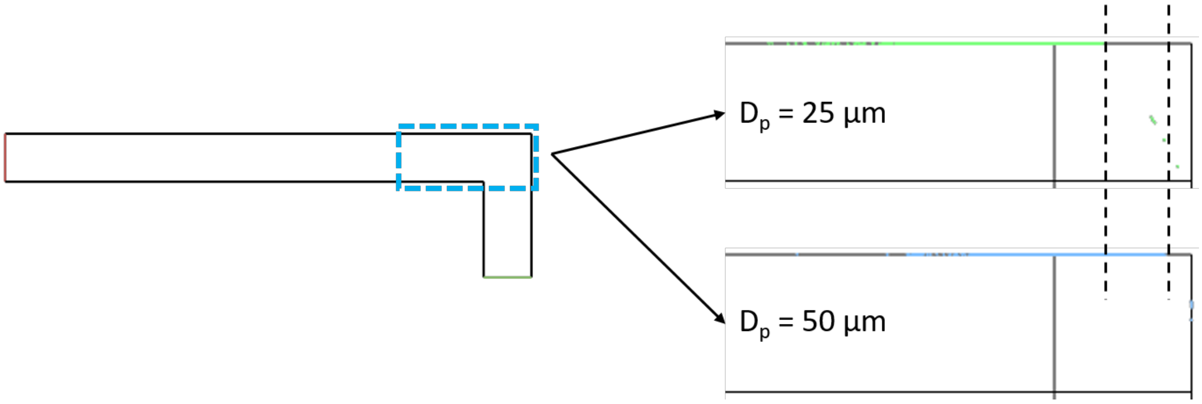

Figure 3.8: Top wall deposition for particle diameters $D_p = 25$ μm (top right) and 50 μm (bottom right) in geometry A, with V_{max} and T = 20°C.

Notice that the filters in the real exhaust begin still in a zone represented in this study by the top wall, 27.5 mm away from the right vertical wall. This means that the further to the left the particle deposition is, the more particles the exhaust is able to capture efficiently. As it was seen earlier in Chapter 1.1, this translates into a better rating for the exhaust performance in grease filter efficiency. This also avoids grease particles dropping out of the exhaust inlet, which might happen when the exhaust is turned off if there is any particle deposition in vertical or near entry walls.

Particles with an intermediate size have a particularity: since the Stokes number is not as small, they deviate to some extent from the streamlines, which means that there is also a possibility to enter the top corner recirculation zone, being higher for bigger particles. However, once there, particles with more mass (higher Stokes number) have higher possibilities to leave the recirculation bubble, as previously mentioned in Chapter 1.2.3. In this balance, turns out to be the particles with $D_p = 20$ μm the most likely to stay inside the bubble, with the particles of diameter $D_p = 50$ μm having a small possibility to end up in the right vertical wall while moving out of the recirculation zone.

The influence of the inlet temperature is also going to be analysed. Table 3.4 presents the results of the particle tracing simulations for all diameters at maximum velocity, V = 2.37 m/s, and for temperatures of 40°C and 60°C.

Table 3.4: Deposition percentages for each diameter in geometry A with V_{max} and T = 40 and 60°C.

D_p	Top Wall	Outlet	Top Corner Recirculation	Left Vertical Wall	Right Vertical Wall
			T = 40°C		
10	0	99.84	0.12	0.04	0
15	0	99.15	0.85	0	0
20	32.65	62.08	5.27	0	0
25	78.31	14.69	7	0	0
50	99.73	0.12	0	0	0.15
100	100	0	0	0	0
			T = 60°C		
10	0	100	0	0	0
15	0	99.31	0.69	0	0
20	26.77	71	2.23	0	0
25	75.69	18.31	6	0	0
50	100	0	0	0	0
100	100	0	0	0	0

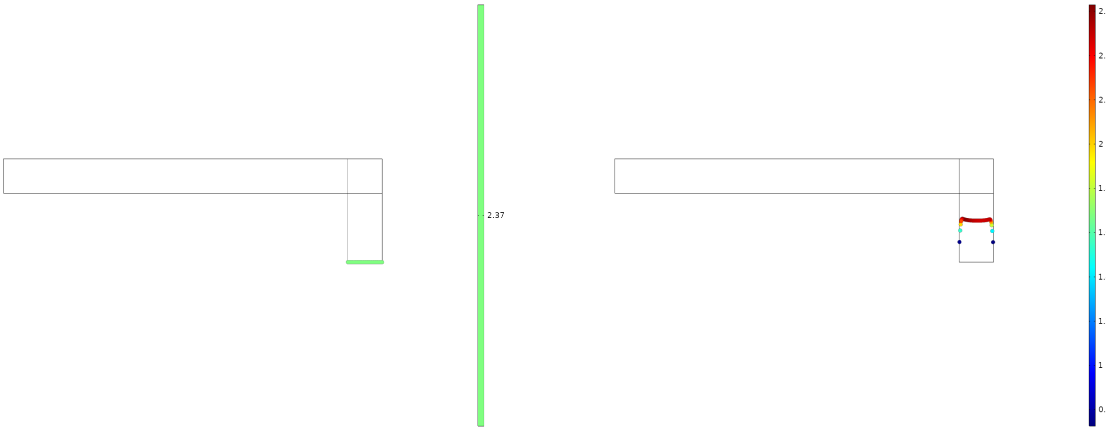

(a) t = 0 s. (b) t = 0.005 s.

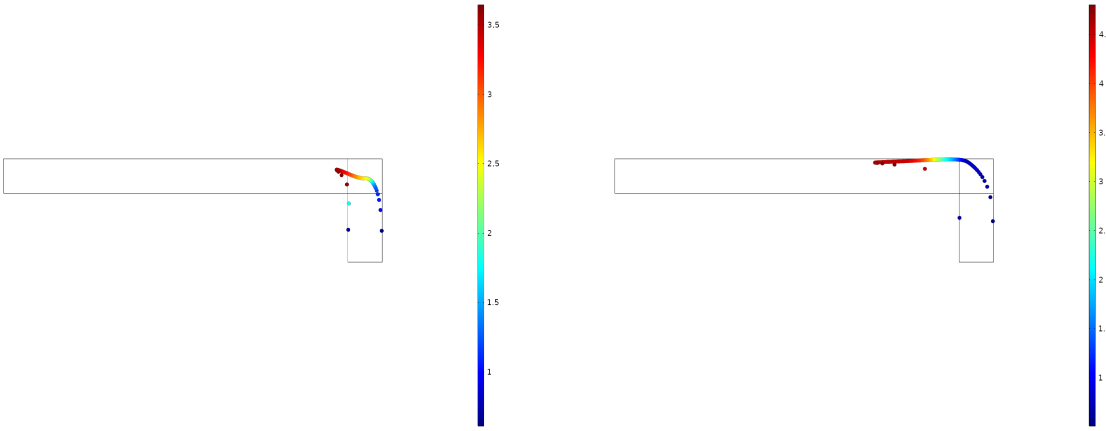

(c) t = 0.01 s. (d) t = 0.015 s.

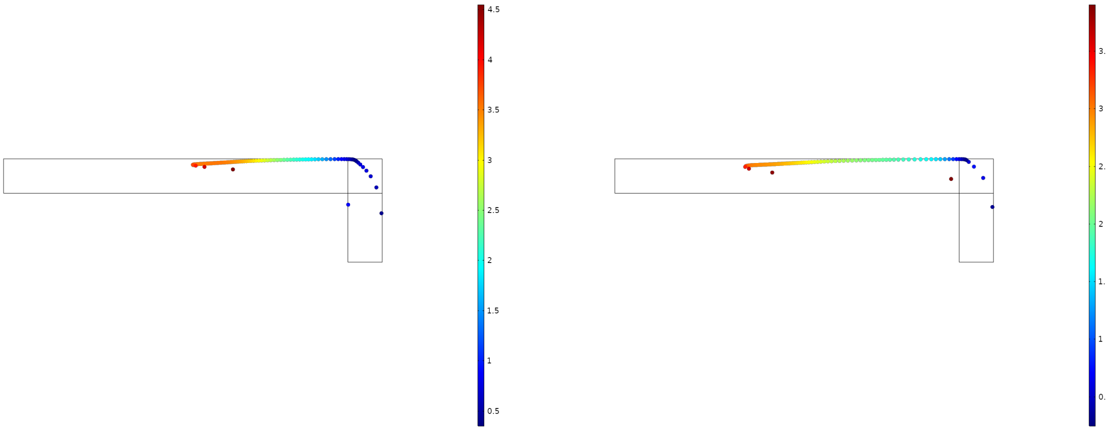

(e) t = 0.02 s. (f) t = 0.025 s.

Figure 3.9: Particle movement evolution throughout the first 0.025 seconds in geometry A, for particles with diameter $D_p = 20$ μm in working temperature T = 40°C and with inlet velocity V_{max}.

Figure 3.9 presents the initial evolution of the particle motion for one of the cases pointed out in Table 3.4, with the color legend displaying the velocity for each particle moving inside the channel. Slower particles near the right vertical wall are the ones most likely to be trapped inside the top corner recirculation zone, which represents 5.27% of the particles in the case shown above.

One conclusion that can be taken immediately by comparing both tables is that the particle diameter has a much more significant dominance to define the deposition position of the particle itself. Nevertheless, the flow temperature still has some impact on the deposition places for the particles, specially for those with a diameter between 15 and 25 μm. Those particles tend slightly more towards the outlet and less towards the top wall as the temperature increases. It is also coherent with the Stokes number, since higher temperatures correspond to higher flow viscosity. This provides a smaller Stokes number which means a bigger inclination for the particles to follow the streamlines. A less dense flow also means it is easier for the particles to escape the recirculation zones, tendency observed as well in the results.

Finally, the influence of the inlet velocity is also studied. Table 3.5 shows the results of the particle tracing simulation for all diameters at the minimum velocity, V = 2.02 m/s, with an inlet ambient temperature (T = 20°C) in geometry A.

Table 3.5: Deposition percentages for each diameter in geometry A with V_{min} and T = 20°C.

D_p	Top Wall	Outlet	Top Corner Recirculation	Left Vertical Wall	Right Vertical Wall
10	0	100	0	0	0
15	0	99.92	0.08	0	0
20	25.08	74.81	0.11	0	0
25	78.08	21.92	0	0	0
50	99.62	0.38	0	0	0
100	99.96	0.04	0	0	0

The results show a tendency by decreasing velocity similar to the one when the inlet temperature was increased to 60°C: much less significant comparing to the particle diameter and a tendency for more particles in the outlet and less in the top wall for the intermediate diameters. However, since the flow velocity is smaller, the number of particles in the top recirculation zone is even smaller, almost null. This also fits with the definition of the Stokes number: a smaller flow velocity results on a smaller Stokes number, which means the particle tendency to move according to the flow streamlines is bigger.

3.2 Geometric Alternatives

In this section, several different geometries were tested in order to improve the results obtained with the initial geometry in terms of pressure losses and particle deposition. Firstly, two new geometries were introduced: B and C. Then, geometry B was improved, creating geometries B15, B20 and B30. Finally, a new version of the exhaust geometry was studied via geometries D and E, being improved via geometries E10, E15, E20 and E30 (these ones not studied in particle tracing for reasons described later on). The mesh on these studies is based on the one made for geometry A, with the size length of 0.1875 mm for the quadrangular elements and smaller for any *mapped mesh* zones.

3.2.1 Pressure losses in the channel

The pressure losses are calculated in the same way here as they were for geometry A: through the local pressure loss coefficient K. In order to obtain conclusions, the emphasis will be rather more on that coefficient than the recirculation zones, although those are still going to be analysed. In order to reduce the computational time spent in all studies and since the results from geometry A allow to verify that there exists a constant pattern between all velocities, studies were made exclusively for the minimum inlet velocity, V = 2.02 m/s, and the maximum inlet velocity, V = 2.37 m/s. However, it was still performed simulations for the same ten inlet temperatures.

Geometries B, C

These two new geometries were created mainly in order to reduce the pressure losses. The idea for both of them was to reduce the recirculation zones and with it, the energy losses of the flow. This was made in different ways: in geometry B the approach was made by reducing the angle in the interior corner of the channel while in geometry C that corner was cut and divided in two smaller consecutive ones, while trying to eliminate the top corner recirculation zone. As it is shown in Figure 3.10 below, that last part was successfully done, presenting only two very small zones of recirculation, which can be neglected due to their small area. It also shows a behaviour similar to geometry A for the temperature fields.

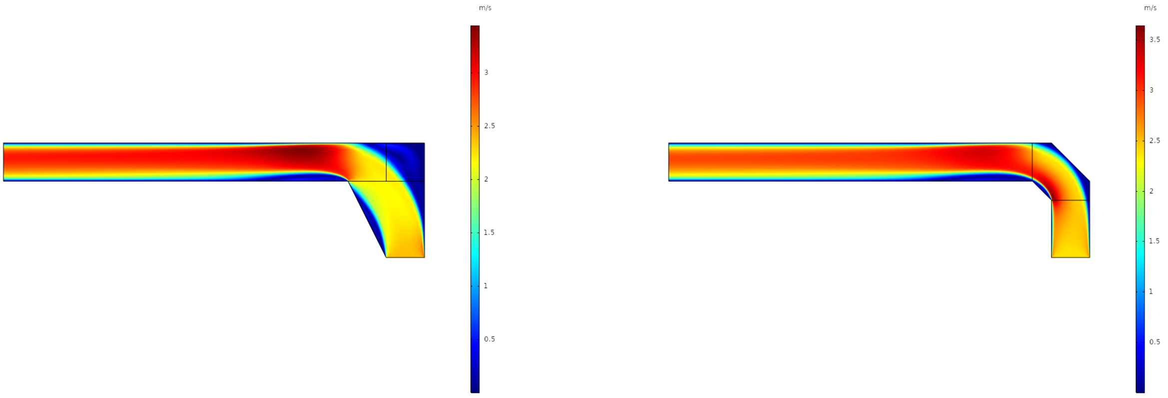

(a) Geometry B velocity results.

(b) Geometry C velocity results.

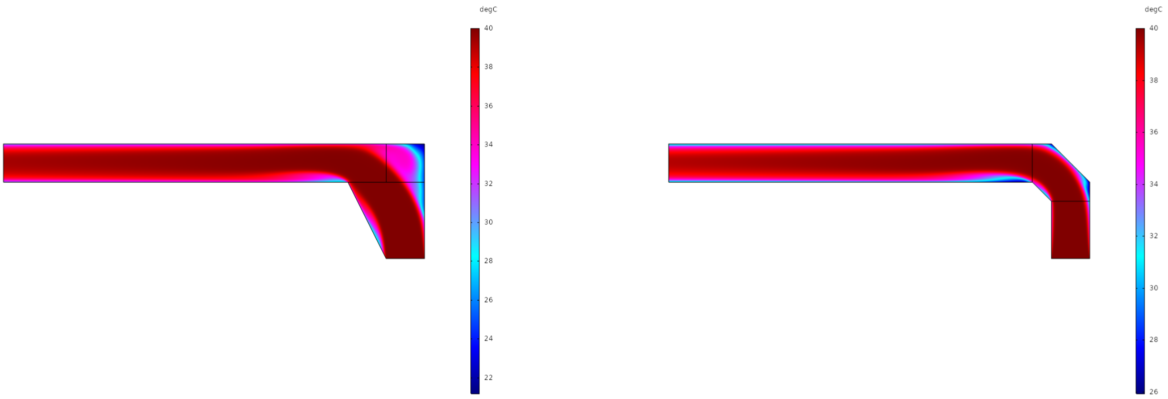

(c) Geometry B temperature results.

(d) Geometry C temperature results.

Figure 3.10: Flow velocities and temperatures for geometries B and C for the case of V_{max} and T = 40°C.

Geometry B, on the other hand, shows a top corner recirculation zone even bigger than the one in geometry A. This was expected, since the wall slope to the left allows the flow to progress earlier to the exit zone, cornering with a less aggressive pressure gradient and leaving a bigger recirculation zone in the area to the right. However, the tendencies are still the same found in geometry A: the recirculation bubble tends to diminish for lower velocities and higher temperatures (Figure 3.11).

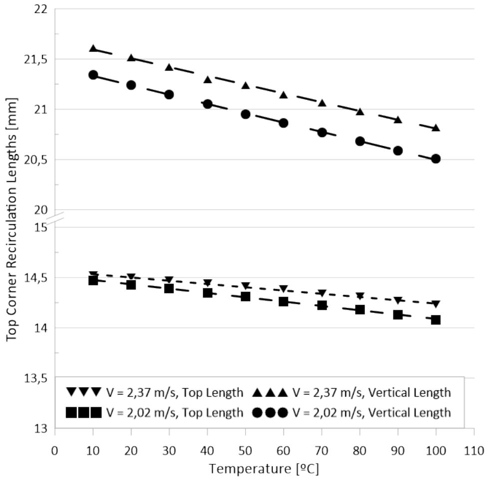

Figure 3.11: Variation of top and vertical recirculation length with the inlet velocity and temperature in geometry B.

Also visible in Figure 3.10 is the bottom recirculation bubble for each geometry. Their area is clearly inferior to the one in geometry A, as it was expected. Figure 3.12 shows that the tendency for the bottom recirculation length to peak at a certain Reynolds number still occurs. However, this now happens at a higher Reynolds number, around 2800 to 2900 for geometry B and over 3350 for geometry C.

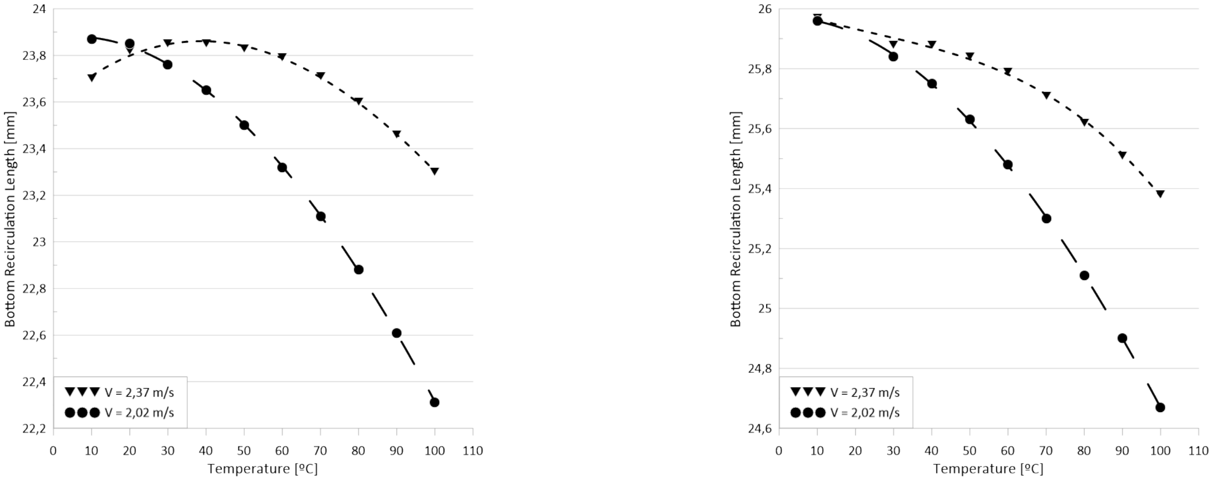

(a) Geometry B.

(b) Geometry C.

Figure 3.12: Variation of bottom recirculation length with velocity and temperature for geometries B, C.

The points for T = 20°C in geometry C are not presented since the result was not converged, due to numerical errors in the simulation. It is observed that the bottom recirculation length is slightly lower for geometry B, an initially unexpected result since the cornering in geometry C is more progressive. However, that geometry has a smaller bottom recirculation height (1.93 mm in geometry C against 2.17 mm in geometry B, for ambient temperature and maximum velocity), which corresponds to the expectation stated above. The tendencies for that value also remain the same from geometry A: a minimal drop with a decrease in velocity (0.05 mm in both cases), with that peak height happening in the same section of the respective geometry, no matter the velocity.

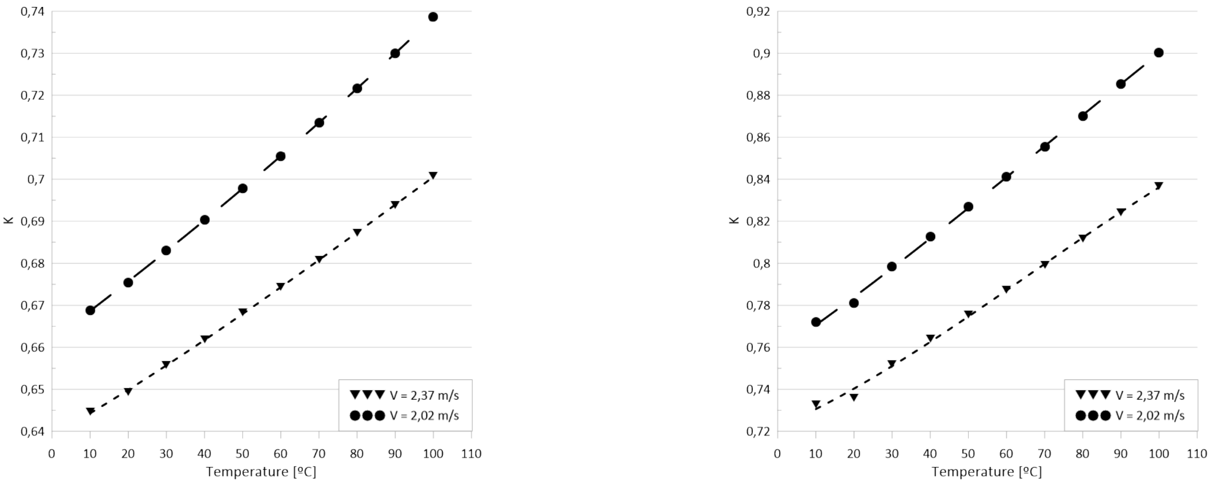

(a) Geometry B. (b) Geometry C.

Figure 3.13: Values of K for geometries B and C and their dependence on temperature and velocity.

The results for the local pressure loss coefficient K in both geometries are presented in the graphs of Figure 3.13, with Figure 3.13(a) being the case for geometry B and Figure 3.13(b) for geometry C. The main conclusion to extract is that with the reduction in the recirculation areas, specially the bottom recirculation zone, the new geometries successfully reduce the value of K. For an inlet temperature of T = 40°C at V_{max}, K decreases from 1.87 (geometry A) to 0.662 in geometry B and 0.690 in geometry C. This shows a great improvement for both cases in terms of energetic efficiency from a small change in the channel geometry. Both cases still maintain the same linear tendencies with velocity and temperature shown in geometry A. However, the most efficient case (with a lower K value) is geometry B. This seems to happen due to the top corner recirculation zone not absorbing a lot of energy from the flow, while geometry C forces the flow to face a bigger angle, bringing a more adverse pressure gradient. It also has more contact with the walls, increasing the viscous losses through them.

Geometry B improvement

Being geometry B the most efficient of the two tested cases, it was chosen to be further improved by increasing the slope of the left entry wall by moving the corner point in the geometry by the number presented in the geometry name, as explained in Chapter 2.2.1, creating geometries B15, B20 and B30.

Since the top corner recirculation zone seems not to absorb much energy from the flow, it is not going to be analysed. However, it is interesting to notice that both lengths in the wall increased from geometry B to B15 (21.30 to 21.71 mm with maximum inlet velocity and T = 40°C), as it was expected due to the angle change in the left entry wall. Nevertheless, for geometries B20 and B30, there was a slight decrease (less than 0.1 mm) compared to the value obtained for the same case in geometry B15. Those geometries, B20 and B30, had nearly equals values, with B30 values just under by 0.01 or 0.02 mm when not the same. It is also worth noticing that the tendencies for the top corner recirculation zone when changing inlet temperature or velocity were maintained.

In these cases, only geometry B15 has a bottom recirculation zone, with a linear tendency across the inlet temperature variation. Its size is quite small comparing to previous geometries, with a length of 7.83 mm and maximum height of 0.37 mm for the case of maximum velocity and temperature of T = 20°C (Figure 3.14).

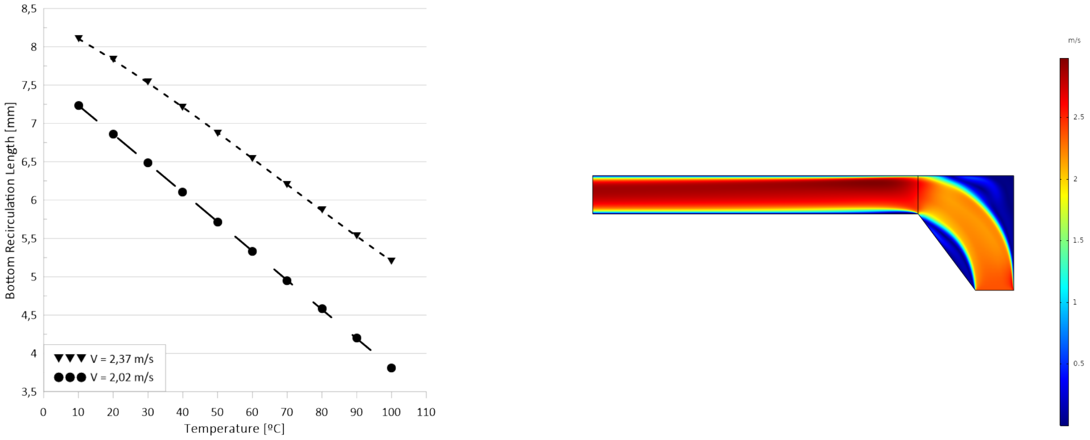

(a) Bottom recirculation length.

(b) Geometry B15 velocity field.

Figure 3.14: Geometry B15 bottom recirculation length and flow velocity for V_{max}, T = 20°C.

For geometries B20 and B30, the bottom recirculation zone does not exist, replaced by another left to the entry. Figure 3.15 shows as well that the only noticeable difference between both geometries is a bigger recirculation zone near the left entry wall for geometry B30, although it only increases by filling an area non-existent in geometry B20, with remaining flow path being nearly the same since the flow starts to behave similarly to a flow in a pipe with the same diameter of the exit zone even before entering that zone. That also happens in geometry B20, hence the disappearance of this recirculation bubble.

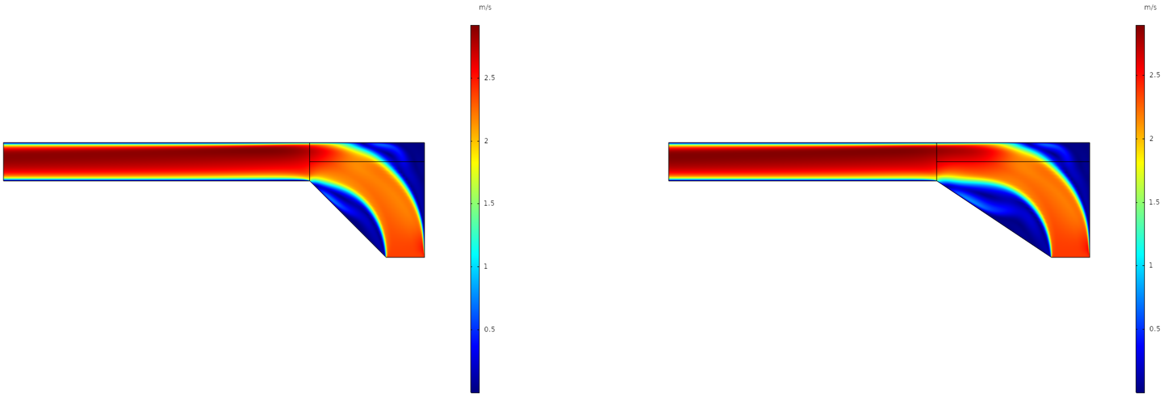

(a) Geometry B20.

(b) Geometry B30.

Figure 3.15: Flow velocities for geometries B20 and B30 for the case of V_{max} and T = 20°C.

However, that flow behaviour on geometry B20 does not come across as desired in terms of values for K. With no recirculation zone in both geometries B20 and B30, the main difference in terms of losses occurs due to the extra 10 mm where the flow is in contact with the walls in the exit zone, meaning that geometry B30 has the upper hand in terms of K. Since the recirculation zone in geometry B15 is quite small, it does not take much energy from the flow. So, the values for K are also better in this case than for geometry B20. However, geometry B30 is still the best case overall, as it can be seen in Figure 3.16, although every case improves on geometry B due to the reduction or elimination of the bottom recirculation zone.

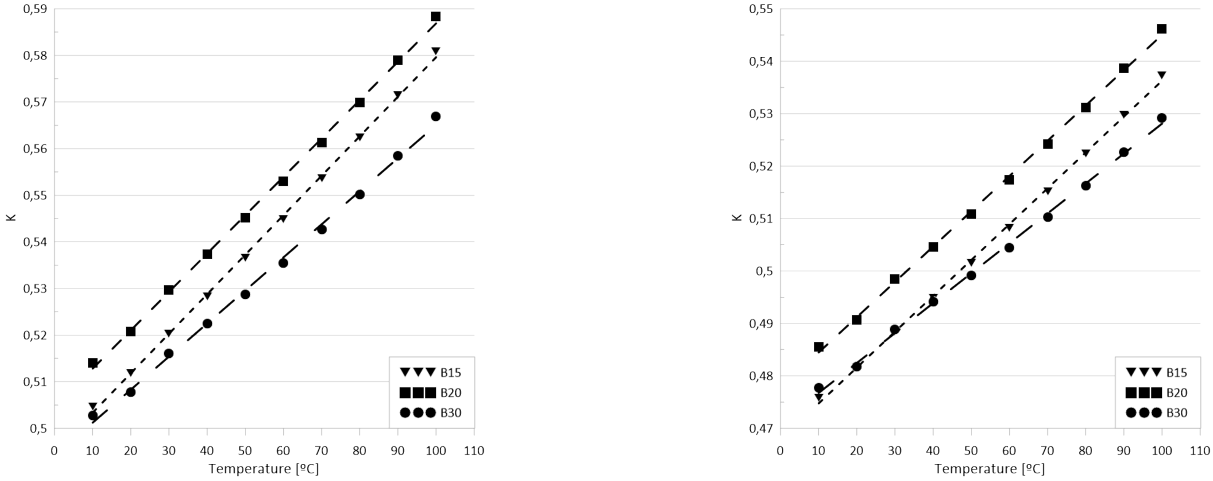

(a) Variation of K for V_{min}.

(b) Variation of K for V_{max}.

Figure 3.16: Values of K for geometries B15, B20 and B30 and the dependence with temperature for both velocities.

Geometries D, E

The new real cases for the exhaust geometry are now presented. Geometry D was still studied but some simulation cases were not converging. Although it was attempted to place the outlet in a similar position for all geometries, it was found that this was preventing the flow to reach a fully developed condition in this geometry, with the bottom recirculation zone being forced to reattach unnaturally soon. Thus, geometry E was designed, allowing the flow to reach a fully developed condition, as it can be seen by the constant wall shear stress value in Figure 3.17(b), in contrast to the non-developed state in Figure 3.17(a). Ergo, only the results for geometry E will be presented.

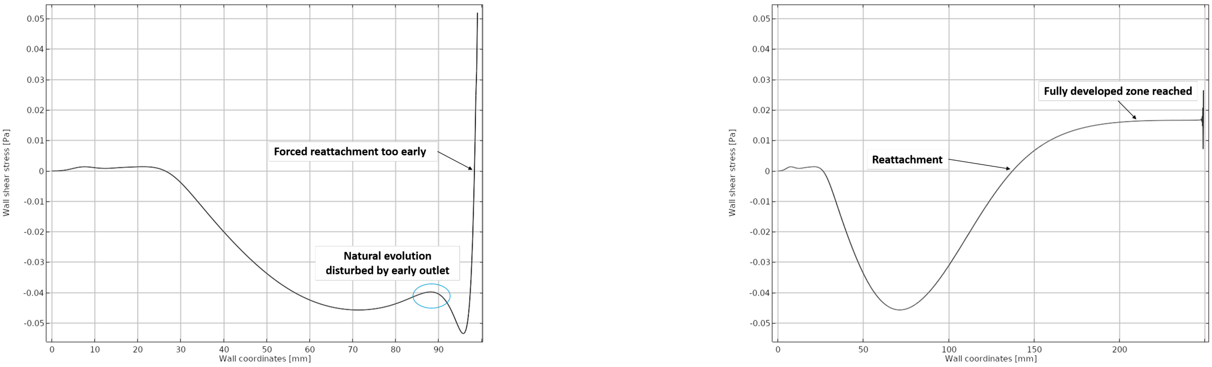

(a) Geometry D, not fully developed.

(b) Geometry E, reaching fully developed.

Figure 3.17: Wall shear stress evolution throughout the bottom wall in geometries D and E.

Figure 3.18 shows the evolution of the top corner (Figure 3.18(a)) and bottom recirculation (Figure 3.18(b)) zones for geometry E.

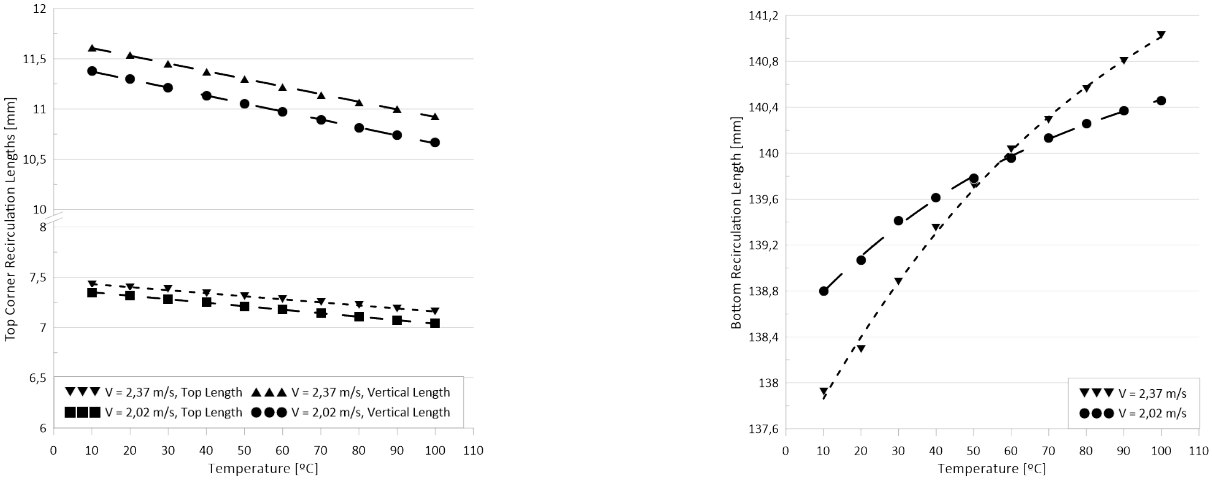

(a) Top corner recirculation zone.

(b) Bottom recirculation zone.

Figure 3.18: Recirculation zone evolution with temperature for geometry E.

Comparing the top corner recirculation zone, it can be seen that the values for the wall lengths are slightly smaller than in geometry A. By removing the bottom wall of geometry A, it also allowed the bottom recirculation height to be smaller, comparing only in the 10 mm height of geometry A's exit zone: from 4.53 mm in geometry A to 4.25 mm in geometry E, for the same case (maximum inlet velocity and inlet temperature of T = 20°C). This allows for the flow to pass through the bottleneck with less resistance and, possibly, less energy losses. It also explains the smaller area in the top corner recirculation zone. However, the removal of the bottom wall and attachment of a new area beneath it increases a lot the area of the bottom recirculation zone compared to geometry A, with the length going from 49.86 to 138.29 mm. This is visible in Figure 3.19 below. The tendencies are similar to geometry A, although the peak is not visible in this range of temperatures, meaning that it should happen in a Reynolds number of 1700 or under.

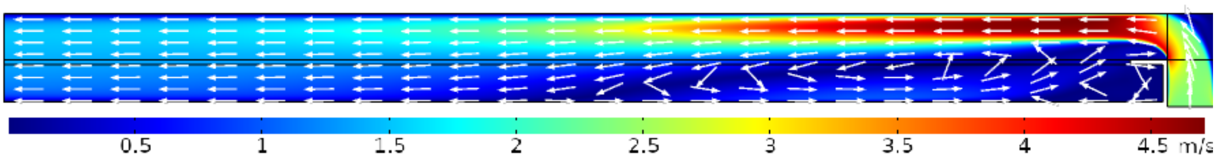

Figure 3.19: Flow velocities in geometry E for a case with V_{max} and T = 40°C.

The values for the local pressure loss coefficient, presented in the graph from Figure 3.20, reflect the discussion about the recirculation zones. The balance between a bottleneck that allows fluid to pass by easily and a bigger bottom recirculation zone results in a K value near, but below the one in geometry A: for an inlet temperature of 20°C and inlet velocity of V = 2.37 m/s, geometry E presents a K of 1.76 while geometry A has a value of 1.84. The values are very close, likely within the numerical uncertainty. The tendencies verified are still the same, with the only difference being a slower evolution of K with the inlet temperature. This behaviour can be partially explained due to the big difference between the geometries in the exit zone and because, since geometry E has a bigger channel height and length, the ratio of channel area to heated surface will be much larger, diminishing the temperature effects in the flow.

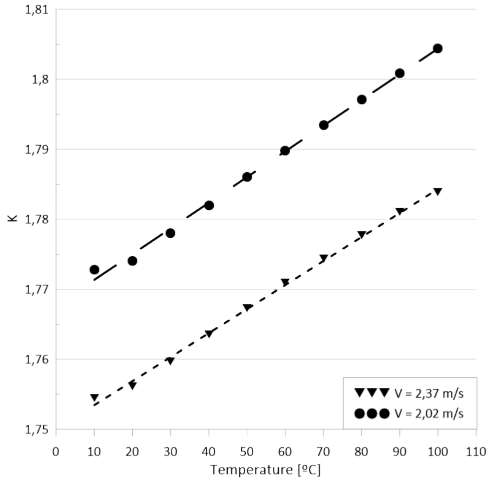

Figure 3.20: Values of K for geometry E and the variation with temperature and velocity.

Studies were made for the optimized versions of geometry E: E10, E15, E20 and E30. The values for recirculation zones were in agreement with the trend anticipated, with the top corner recirculation lengths increasing in about 3 mm and bottom recirculation area also decreasing considerably, with the length cut down by around 50 mm. However, the results for the local pressure loss coefficient K were off from expected and far from any credible values since the simulations did not converge. For this reason, the results for these geometries will not be presented in this work, neither there will be any results for the same geometries in the following section.

3.2.2 Particle tracing

In this section, the particle deposition will be studied for each of the optimized geometries already analysed in the previous section. It will also be made a balance, if necessary, between the pressure loss and the particle tracing results to reach a conclusion to which geometry brings the best overall performance to the exhaust. The results will be focused more on the inlet temperature of 40°C, since that was the measured temperature in a real case, but the tendencies will also be revealed.

Geometries B, C

Since the study is performed for a two-phase flow, the new geometries had to be studied as well in terms of particle deposition. However, since the geometries have changed, the wall naming also underwent some modifications. Figure 3.21 presents the wall identifications for geometries B and C. Following the schematic figure, Table 3.6 displays the distribution of the particle depositing in the walls for geometries A, B and C, with an inlet temperature of 40°C and maximum velocity V = 2.37 m/s. This allows for a better comparison between the performance of the three geometries.

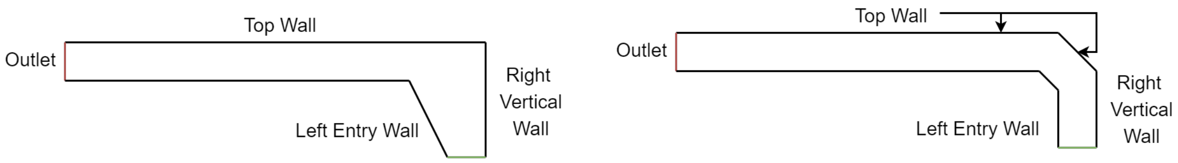

(a) Geometry B.

(b) Geometry C.

Figure 3.21: Wall nomenclature used for the particle tracing study analysis of geometries B and C.

Table 3.6: Deposition percentages for geometries A, B and C with V_{max} and T = 40°C.

D_p	Top Wall	Outlet	Top Corner Recirculation	Left Entry Wall	Right Vertical Wall
Geometry A					
10	0	99.84	0.12	0.04	0
15	0	99.15	0.85	0	0
20	32.65	62.08	5.27	0	0
25	78.31	14.69	7	0	0
50	99.73	0.12	0	0	0.15
100	100	0	0	0	0
Geometry B					
10	0	99.54	0.46	0	0
15	0	98.38	1.62	0	0
20	0	92.62	7.38	0	0
25	22	64.46	13.54	0	0
50	98.96	1.04	0	0	0
100	100	0	0	0	0
Geometry C					
10	0	100	0	0	0
15	0	100	0	0	0
20	0	100	0	0	0
25	31.54	68.46	0	0	0
50	99.35	0.65	0	0	0
100	100	0	0	0	0

Both new geometries have the intended effect on the particle deposition: less particles end up in the walls and more in the outlet, and therefore, in the exhaust filter. This can be noticed very clearly particularly for the particle with a diameter of 20 μm, where with geometry A almost a third would to the top wall but with geometries B and C all of them (or almost, for the case of geometry B) go to the outlet. Another noticeable trend is the increase of particles in the top corner recirculation zone for geometry B. This happens due to the increase in area for this recirculation bubble, expanding to the left of the entry zone, hence managing to capture particles easily and in bigger quantities. Despite that, the numbers presented should not be taken as 100% accurate or consistent due to the randomness of the turbulent flow, which might provoke the particles to be deposited in the walls near the recirculation zone or release them from the bubble and direct them to the outlet. Nevertheless, the existence of this recirculation zone causes geometry C to have a slightly bigger percentage of particles on the outlet for some cases, since that geometry eliminates the bubble manifested in geometry B, replaced by two small negligible ones. However, geometry C has a higher percentage of particles on the top wall, with the particles of geometry B being deposited more to the left, that is, closer to the zone where the filter begins in the real exhaust (Figure 3.22).

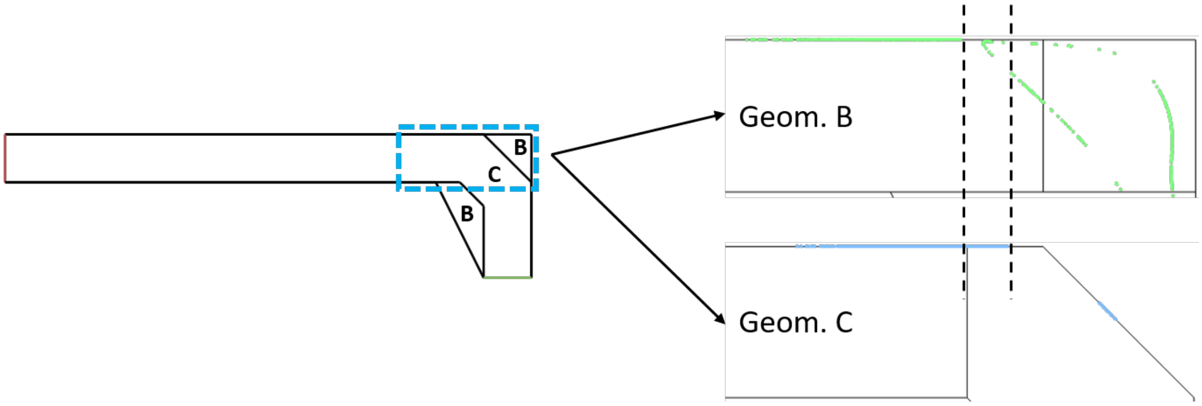

Figure 3.22: Top wall deposition in geometries B (top right) and C (bottom right) for $D_p = 25$ μm with V_{max} and T = 40°C.

Although it is not expressed in the previous table, both geometry B and C keep the same tendencies from the initial geometry: the particle diameter is still the dominant property when it comes to their depositing position, keeping lighter particles more orientated to the outlet and heavier ones to the top walls. Velocity and temperature are still also a secondary factor to be taken into account, with lower inlet velocities and higher working fluid temperatures pushing the particles away from the walls and to the outlet. All of this acts in accordance to the expected by the definition of the Stokes number, as it was explained for the case of geometry A (Chapter 3.1.2). Taking all of the previous inputs into consideration, it is concluded that geometry B has a better performance not only on an energetic level but also in terms of grease filtering efficiency compared to geometries A and C.

Geometry B improvement

For geometries B15, B20 and B30, it is used the same wall nomenclature as in geometry B, since all have a similar shape. Table 3.7 presents the deposition results from the study for these three geometries, with an inlet temperature of 40°C and maximum velocity V = 2.37 m/s, for all particle diameters.

By increasing on the top corner recirculation area from geometry B, with the increment on the left entry wall angle, the amount of particles entering the recirculation zone suffered a small increment. The pressure gradient affecting the flow also ends up being slightly reduced. This results in more particles going to the outlet and less particles deposited in the top wall for all the three geometries compared to geometry B, with the cases for geometries B20 and B30 being quite similar, depending on the particle diameter since the flow goes through a similar path due to the disappearance of the bottom recirculation zone. Again, all previous tendencies for the particle deposition with particle diameter, flow inlet velocity and temperature were maintained and coherent with the Stokes number influence on the particle movement.

Although geometry B20 might have a small advantage in terms of particle deposition, it is the worse of the three geometries for pressure losses. Therefore, balancing the results from the fluid flow with the particle tracing study, the conclusion drawn from the results is that geometry B30 is, from all the geometries studied in this work, the best case obtained for the two-phase flow of the exhaust.

Table 3.7: Deposition percentages for geometries B15, B20 and B30 with V_{max} and T = 40°C.

D_p	Top Wall	Outlet	Top Corner Recirculation	Left Entry Wall	Right Vertical Wall
Geometry B15					
10	0	99.38	0.62	0	0
15	0	97.69	2.31	0	0
20	0	91.65	8.35	0	0
25	10.11	71.85	18.04	0	0
50	98.46	1.54	0	0	0
100	100	0	0	0	0
Geometry B20					
10	0	99.88	0.12	0	0
15	0	98.23	1.77	0	0
20	0	91.15	8.85	0	0
25	2.92	78.19	18.89	0	0
50	99.81	0.19	0	0	0
100	100	0	0	0	0
Geometry B30					
10	0	99.88	0.12	0	0
15	0	98.08	1.92	0	0
20	0	91.04	8.96	0	0
25	5.77	74.73	19.5	0	0
50	98.88	1.12	0	0	0
100	99.96	0.04	0	0	0

Geometry E

For the new real cases of exhaust geometries, only geometry E was studied for reasons previously explained. The wall nomenclature can be seen below in Figure 3.23.

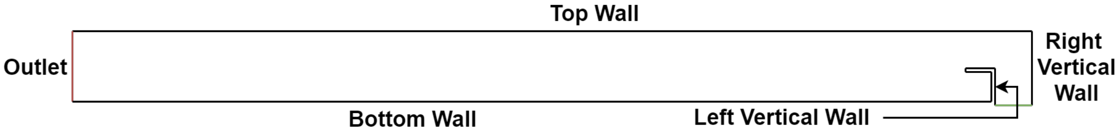

Figure 3.23: Wall nomenclature used for the particle tracing study analysis of geometry E.

The main difference on the flow motion from geometry A to E, beyond the increase in the bottom recirculation length and the flow expansion in the exit zone, is the reduction in the bottom recirculation height, enlarging the passage zone for the flow in the bottleneck zone after the corner. This reduces the mass flow passing closer to the top wall, thus reducing the amount of deposition in the top wall while more particles are directed to the outlet, as intended. This comparison can be seen clearly in Figure 3.24, where it is shown the particle deposition for particles diameters of 20 (Figure 3.24(a)) and 25 μm (Figure 3.24(b)) for both geometry A and E, at a working temperature of T = 40°C and with inlet velocity V_{max}. Both cases show that from geometry A (blue) to geometry E (green) exists a decrease in the top wall deposition (lighter colors) and an increase in the outlet deposition (darker colors) of around 10%.

Due to the flow expansion caused by the height growth in the exit zone of the geometry, a very small amount of lighter particles ended up in the bottom wall for the simulations of geometry E. However, this is less likely to happen in the real exhaust because further ahead in the channel, the flow can start to be affected by an upstream from the exhaust pipe which will affect the particle movement, preventing the

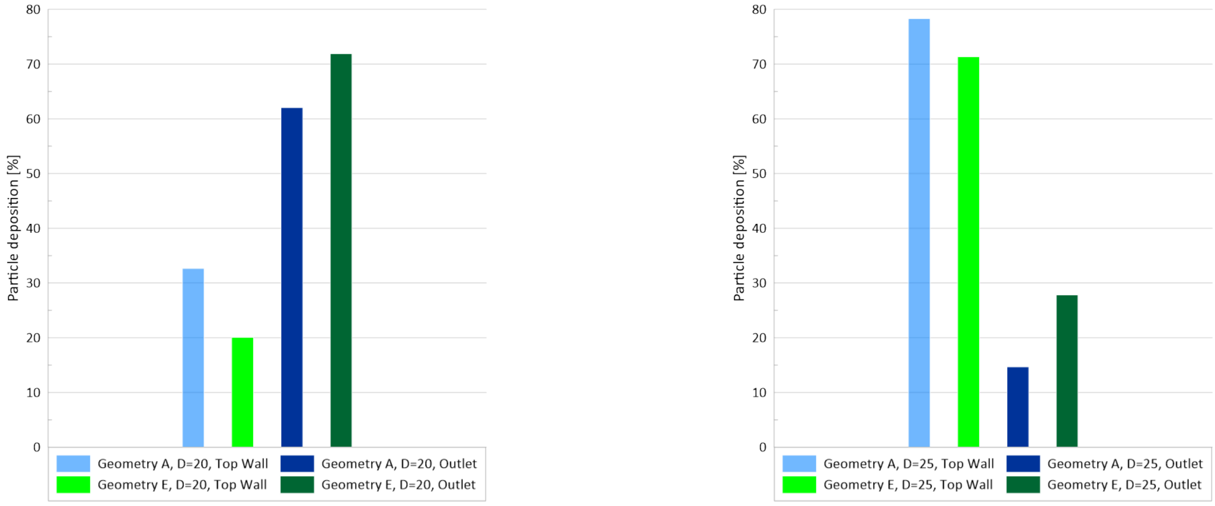

(a) Deposition for $D_p = 20\ \mu$m.

(b) Deposition for $D_p = 25\ \mu$m.

Figure 3.24: Particle deposition for top wall and outlet for geometries A, E with V_{max} and T = 40°C.

direct deposition in the bottom wall. This should then only happen in situations were gravity acts on the particles that collided on the top wall, after the exhaust was used and when there is no flow being pulled by the fan. Table 3.8 shows more in detail the numbers for the several particle deposition locations in geometry A and E, for all particle diameters, in the same case with an inlet temperature of 40°C and maximum velocity V = 2.37 m/s. Note that all of the previously mentioned tendencies for property influence in particle movement and Stokes number were also kept in this case.

Table 3.8: Deposition percentages for geometries A and E with V_{max} and T = 40°C.

D_p	Top Wall	Outlet	Top Corner Recirculation	Left Vertical Wall	Right Vertical Wall	Bottom Wall
			Geometry A			
10	0	99.84	0.12	0.04	0	0
15	0	99.15	0.85	0	0	0
20	32.65	62.08	5.27	0	0	0
25	78.31	14.69	7	0	0	0
50	99.73	0.12	0	0	0.15	0
100	100	0	0	0	0	0
			Geometry E			
10	0	99.38	0.54	0	0	0.08
15	0	98.65	1.35	0	0	0
20	20.08	71.92	8	0	0	0
25	71.35	27.81	0.84	0	0	0
50	99.88	0.12	0	0	0	0
100	100	0	0	0	0	0

From this study, together with the small improvement in the values of K, it shows that the new geometry already implemented in the real exhaust might benefit the system. Although it does not perform better than the previous changes from this work, it shows that there exists potential to out-perform them by applying similar improvements.

3.3 Experimental Tests

To evaluate the numerical results from the studies performed in this work, it was carried out an experimental study as well. This was made in the acrylic prototype describe in Chapter 2.3, simulating the case of geometry B. Since only the minimum and maximum velocities ($V_{min} = 2.02$ and $V_{max} = 2.37$ m/s, respectively) were studied in the numerical part of this geometry, these were also the only cases tested experimentally. The tests were also performed at an ambient temperature around 25°C, being comparable to the inlet temperature of 20°C studied numerically.

The tests were performed in two different ways: the *single tube* method, where the data is retrieved by only one pitot tube in the outlet zone (similar to the tests conducted by Ferro [4]), and the *double tube* method, were pressure is measured both at the inlet and in the fully developed section. The graph below (Figure 3.25) displays the results for the local pressure loss coefficient K dependence on velocity on both cases and the numerical case as well.

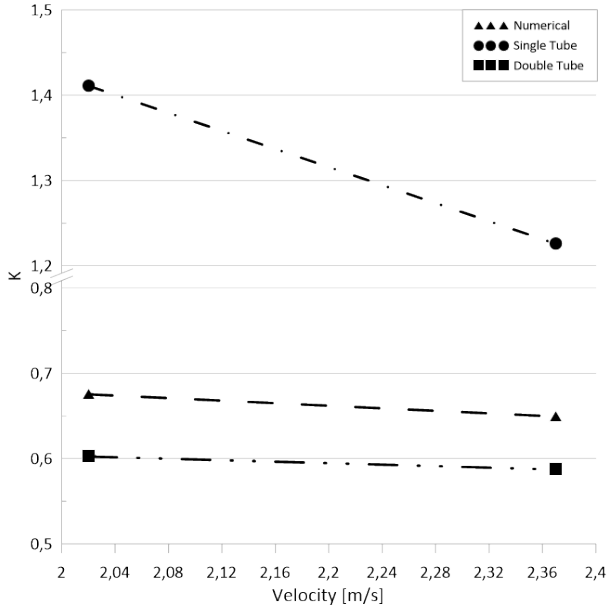

Figure 3.25: Values of K for experimental tests and numerical solution of geometry B at T = 20°C.

The results show the double tube method much closer to the numerical results than the single tube method, both for the dependence of K with velocity (with a much similar slope) and in terms of values, since the single tube method takes into account the dynamic pressure by considering atmospheric pressure at the inlet. This shows that assuming that the entry pressure is near the atmospheric pressure is an incorrect premise, leading to unexpectedly large values of K. The single tube method results are, however, coherent with the tests executed by Ferro since the values obtained numerically are around twice as high for geometry B but also for geometry A, the case tested in that said work.

Comparing the results for the double tube method with the numerical, it looks that the simulations have similar results, keeping the tendency of a decreasing K value with the increase of the inlet velocity. Nonetheless, the numerical solution is overestimating the results of the experimental tests by around 10%. However, that is within the expected error range of the sensor for pressure values of this order (relative pressure to the atmospheric under 5 Pa). It should also be taken into account that, since the VARIAC works with an analog interface scale, the precision of the power used to control the flow velocity was far from ideal. The placing of the pitot tube at the inlet was also under optimized since the setup was initially planned for a single tube mounting. This caused the tube to be fixed with tape, which had to be replaced frequently in order to avoid the tube placed at an undesired angle or position.

Nevertheless, the results being quite similar from the experimental to the numerical part of the work represents an improvement on previous works and the confirmation that the solutions can be correlated from numerical testing to reality.

Chapter 4

Conclusions

This work had as an objective to improve the performance of a perimetric exhaust both on its energetic performance as well as on the grease filtering efficiency. For that, numerical studies were performed to a variety of new geometries in order to improve the initial geometry, reducing the energy lost in the flow and directing the grease particles to the exhaust filters, while taking into account the effects of the inlet velocity and working temperature of the flow. An experimental study was also performed for one of the geometries so the quality of the numerical simulations could be assessed.

The temperature of the flow entering the exhaust does have an influence on its functioning. Higher working temperatures result on a poorer energetic performance but in an increase on the grease filtering efficiency. The decrease in the inlet velocity has the same effect on energetic and grease filtering as the temperature increase, which is consistent with results from previous studies.

In the particle tracing studies, it was concluded that the property with more influence on the particle movement was the particle diameter. An increase on the particle size would cause it not to follow the flow streamlines as easily, with almost all of the heavier particles ending up on the top wall of the exhaust. On the other hand, a lighter particle follows perfectly the streamline, ending up in the filter most of the times. For the particles with intermediate sizes, working temperature and inlet velocity were decisive, with a temperature increase and velocity decrease favouring the particle movement towards the exhaust filter, represented in this study by the outlet.

Both geometry B and C, the first pair of geometries studied, have a considerably better performance than the initial geometry: the local pressure loss coefficient K values went down as much as three times for some of the studied cases and the number of particles in the outlet zone increase considerably for some particle diameters. However, it was geometry B that had the upper hand of the two, with an inferior K value and a slightly better capability to direct the particles to the filter area.

In order to improve geometry B, three modified versions were created from that foundation: geometries B15, B20 and B30. Although their evolution in performance wasn't linear with the increase in the slope of the wall throughout the versions, all of them were an improvement from the original geometry B. Geometries B20 and B30 were quite similar in terms of grease filtering efficiency due to the disappearance of the bottom recirculation zone present in every other geometry iteration but a lower energetic efficiency caused geometry B20 to be the worst of these final three geometry variations, with geometry B30 being the best performer energetically and, therefore, the overall best geometry studied in this work.

A new real case geometry was also studied in geometry E. Compared to the initial geometry A, a small improvement was found for the values of K, within the margin of numerical uncertainties, but with less dependence on the working temperature of the flow. It also improved slightly the grease filter efficiency, with a higher percentage of particles moving to the outlet due to a less narrow useful area for the flow to pass after the corner. This brings hope for the results of an improved version of this geometry to be even better than the ones obtained in the improved version of geometry B.

Finally, an experimental test was performed to a flow passing through an acrylic prototype channel with a corner based on geometry B. It was settled that the inlet pressure should also be measured instead of assuming atmospheric pressure at the entry, not taking into account the dynamic pressure at the entry. This test also confirmed the reliability of the numerical results, since the solutions obtained for both cases were similar.

Ending, it can be affirmed that the exhaust geometry improvement was accomplished, with the results suggesting that it is possible to obtain a significant improvement to the performance of the perimetric exhaust.

4.1 Future Work

To follow this work, several paths can be taken in order to confirm the results obtained.

A 3D study of the exhaust with these geometry changes, both experimentally and numerically, would be best way to confirm the reliability of the results. However, it is recognized by the author that it would be a very difficult work to perform.

Hence, the continuation of the experimental work is advised. Pressure measurements for different geometries is recommended, with PIV testing being an essential tool for an even better understanding of the flow behaviour for each of the cases. The measurements should also be made with a more precise pressure sensor, in order to reduce any errors in the data gathered. Testing the particle deposition experimentally is also advised, in order to complement the numerical part of this study.

The simulations of the improved new real case geometry should also be studied to see if it is possible to obtain realistic results, since that can bring even better results for the exhaust performance. Conducting the numerical simulations with different turbulence models is also proposed, in order to verify if any changes, including transition effects, can occur and influence the results.

Bibliography

[1] C. D. R. N. 65/2014. Supplementing directive 2010/30/EU of the European Parliament and of the Council with regard to the energy labelling of domestic ovens and range hoods. Official Journal of the European Union, 2013.

[2] C. R. N. 66/2014. Implementing Directive 2009/125/EC of the European Parliament and of the Council with regard to eco-design requirements for domestic ovens, hobs and range hoods. Official Journal of the European Union, 2014.

[3] Teka DPE 90 Model. Image perimetric exhaust. URL `http://www.teka.pt/products/view/21870-hoods-dpe_90`. Online; accessed 20-October-2019.

[4] A. Ferro. Flows in suction channels of air exhausts. Master's thesis, Instituto Superior Técnico, University of Lisbon, 2018.

[5] I. Monteiro. Kitchen Exhauster channel numerical study and optimisation. Master's thesis, Instituto Superior Técnico, University of Lisbon, 2019.

[6] F. M. White. *Fluid Mechanics*. McGraw-Hill, 7th edition, 2011. ISBN 978-0-07-352934-9.

[7] Z. R. Shu and Q. S. Li. An experimental investigation of surface pressures in separated and reattaching flows: effects of freestream turbulence and leading edge geometry. *Journal of Wind Engineering and Industrial Aerodynamics*, 165(December 2016):58–66, 2017.

[8] V. de Brederode. *Aerodinâmica Incompressível : Fundamentos*. IST Press, 1st edition, 2014. ISBN 978-989-8481-32-0.

[9] J. Garcia. Experimental and Numerical Characterization of a Kitchen Range Hood. Master's thesis, Instituto Superior Técnico, University of Lisbon, 2016.

[10] T. H. Kuehn, B. a. Olson, J. W. Ramsey, J. M. Rocklage, and D. Gross. Characterization of effluents from additional cooking appliances. Technical report, 2007.

[11] C. He, L. Morawksa, and D. Gilbert. Particle deposition rates in residential houses. *Journal of the American Academy of Dermatology*, 57(6):3891–3899, 2005.

[12] M. Losurdo. *Particle Tracking and Deposition from CFD Simulations using a Viscoelastic Particle Model*. PhD thesis, 2009.

[13] A. Vié, H. Pouransari, R. Zamansky, and A. Mani. Comparison between Lagrangian and Eulerian methods for the simulation of particle-laden flows subject to radiative heating. *Center for Turbulence Researh, Annual Research Brief*, (i):15–25, 2014.

[14] A. C. Lai and W. W. Nazaroff. Modeling indoor particle deposition from turbulent flow onto smooth surfaces. *Journal of Aerosol Science*, 31(4):463–476, 2000.

[15] G. G. Katul, T. Grönholm, S. Launiainen, and T. Vesala. Predicting the dry deposition of aerosol-sized particles using layer-resolved canopy and pipe flow analogy models: Role of turbophoresis. *Journal of Geophysical Research Atmospheres*, 115(12):1–17, 2010.

[16] H. Åkerstedt. Deposition of submicron charged particles in turbulent pipe flow with an application to the trachea. *International Journal of Multiphysics*, 12(1):9–25, 2018.

[17] H. Åkerstedt. Deposition of Submicron Charged Spherical Particles in the Trachea of the Human Airways . 2012.

[18] J. S. Lin, C. J. Tsai, and C. P. Chang. Suppression of particle deposition in tube flow by thermophoresis. *Journal of Aerosol Science*, 35(10):1235–1250, 2004.

[19] A. Trouvé, B. Cuenot, and D. E. Riber. Numerical modeling of the deposition of combustion-generated soot particles on cold wall surfaces. *Center for Turbulence Research, Proceedings of the Summer Program 2012*, pages 419–428, 2012.

[20] J. S. Lin and C. J. Tsai. Thermophoretic deposition efficiency in a cylindrical tube taking into account developing flow at the entrance region. *Journal of Aerosol Science*, 34(5):569–583, 2003.

[21] V. Loisel, M. Abbas, O. Masbernat, and E. Climent. The effect of neutrally buoyant finite-size particles on channel flows in the laminar-turbulent transition regime. *Physics of Fluids*, 25(12), 2013.

[22] Z. Zhang and Q. Chen. Prediction of particle deposition onto indoor surfaces by CFD with a modified Lagrangian method. *Atmospheric Environment*, 43(2):319–328, 2009.

[23] Y. S. Cheng. Wall deposition of Radon Progeny and Particles in a Spherical Chamber. *Aerosol Science and Technology*, 27(2):131–146, 1997.

[24] A. C. Lai and Y. W. Ho. Spatial concentration variation of cooking-emitted particles in a residential kitchen. *Building and Environment*, 43(5):871–876, 2008.

[25] Z. Zhang and Q. Chen. Comparison of the Eulerian and Lagrangian methods for predicting particle transport in enclosed spaces. *Atmospheric Environment*, 41(25):5236–5248, 2007.

[26] B. Carasi. Compressibility Options and Buoyancy Forces for Flow Simulations. URL `https://www.comsol.eu/blogs/compressibility-options-and-buoyancy-forces-for-flow-simulations`. Online; accessed 27-September-2019.

[27] J. Ferziger and M. Peric. *Computational Methods for Fluid Dynamics.* Springer-Verlag GmbH, 3rd edition, 2002. ISBN 3-540-42074-6.

[28] L. Tian and G. Ahmadi. Particle deposition in turbulent duct flows-comparisons of different model predictions. *Journal of Aerosol Science*, 38(4):377–397, 2007.

[29] COMSOL Multiphysics. COMSOL Multiphysics® User's Guide, 2012.

[30] P. Naphon and J. Suwagrai. Effect of curvature ratios on the heat transfer and flow developments in the horizontal spirally coiled tubes. *International Journal of Heat and Mass Transfer*, 50(3-4): 444–451, 2007.

[31] COMSOL Multiphysics. Heat Transfer Module User's Guide, 2018.

[32] V. Dippold. Investigation of Wall Function and Turbulence Model Performance within the Wind Code. *43rd AIAA Aerospace Sciences Meeting and Exhibit - Meeting Papers*, 2005.

[33] COMSOL Multiphysics. Particle Tracing Module User's Guide, 2018.

[34] A. Giusti, F. Lucci, and A. Soldati. Influence of the lift force in direct numerical simulation of upward/downward turbulent channel flow laden with surfactant contaminated microbubbles. *Chemical Engineering Science*, 60(22):6176–6187, 2005.

[35] I. Lashgari, F. Picano, W. P. Breugem, and L. Brandt. Channel flow of rigid sphere suspensions: Particle dynamics in the inertial regime. *International Journal of Multiphase Flow*, 78:12–24, 2016.

[36] A. Dehbi. Turbulent particle dispersion in arbitrary wall-bounded geometries: A coupled CFD-Langevin-equation based approach. *International Journal of Multiphase Flow*, 34(9):819–828, 2008.

[37] C. J. Tsai, J. S. Lin, S. G. Aggarwal, and D. R. Chen. Thermophoretic Deposition of Particles in Laminar and Turbulent Tube Flows. *Aerosol Science and Technology*, 38(2):131–139, 2004.

[38] A. Turgut, I. Tavman, and S. Tavman. Measurement of Thermal Conductivity of Edible Oils Using Transient Hot Wire Method. *International Journal of Food Properties*, 12(4):741–747, 2009.

[39] A. Bhatia. Fundamentals of Kitchen Ventilation. 228, 2012.

[40] Sensirion. Sensirion SDP1000 Low Range Differential Pressure Sensor Datasheet, 2017.